

Learning to Assist Different Wearers in Multitasks: Efficient and Individualized Human-In-the-Loop Adaptation Framework for Lower-Limb Exoskeleton

Yu Chen, Shu Miao, Gong Chen, Jing Ye, Chenglong Fu, Bin Liang, Shiji Song, and Xiang Li

Abstract—One of the typical purposes of using lower-limb exoskeleton robots is to provide assistance to the wearer by supporting their weight and augmenting their physical capabilities according to a given task and human motion intentions. The generalizability of robots across different wearers in multiple tasks is important to ensure that the robot can provide correct and effective assistance in actual implementation. However, most lower-limb exoskeleton robots exhibit only limited generalizability. Therefore, this paper proposes a human-in-the-loop learning and adaptation framework for exoskeleton robots to improve their performance in various tasks and for different wearers. To suit different wearers, an individualized walking trajectory is generated online using dynamic movement primitives and Bayes optimization. To accommodate various tasks, a task translator is constructed using a neural network to generalize a trajectory to more complex scenarios. These generalization techniques are integrated into a unified variable impedance model, which regulates the exoskeleton to provide assistance while ensuring safety. In addition, an anomaly detection network is developed to quantitatively evaluate the wearer's comfort, which is considered in the trajectory learning procedure and contributes to the relaxation of conflicts in impedance control. The proposed framework is easy to implement, because it requires proprioceptive sensors only to perform and deploy data-efficient learning schemes. This makes the exoskeleton practical for deployment in complex scenarios, accommodating different walking patterns, habits, tasks, and conflicts. Experiments and comparative studies on a lower-limb exoskeleton robot are performed to demonstrate the effectiveness of the proposed framework.

Index Terms—Lower-limb exoskeleton, proprioceptive sensors, multitask walking, online adaptation to wearers.

I. INTRODUCTION

Lower-limb exoskeletons have been applied across various domains, such as industry [1], military [2], and rehabilitation [3]. Various prototypes and commercial products, e.g., ReWalk [4], Ekso [5] and HAL [6] have been developed to address different needs. The primary objective of a lower-limb exoskeleton robot varies depending on its application. For assistive exoskeletons, the goal is often to support the body weight of the wearer and enhance their physical capabilities

Y. Chen, S. Miao, B. Liang, S. Song and X. Li are with the Department of Automation, Tsinghua University, China. G. Chen and J. Ye are with the Shenzhen MileBot Robotics Co., Ltd, China. C. Fu is with the Department of Mechanical and Energy Engineering, Southern University of Science and Technology, Shenzhen 518055, China. This work was supported in part by the Science and Technology Innovation 2030-Key Project under Grant 2021ZD0201404, in part by the Institute for Guo Qiang, Tsinghua University, in part by Shenzhen Science and Technology Program under grant KQTD20200909114235003, and in part by the National Natural Science Foundation of China under Grant U21A20517 and 52075290. Corresponding author: Xiang Li (xiangli@tsinghua.edu.cn)

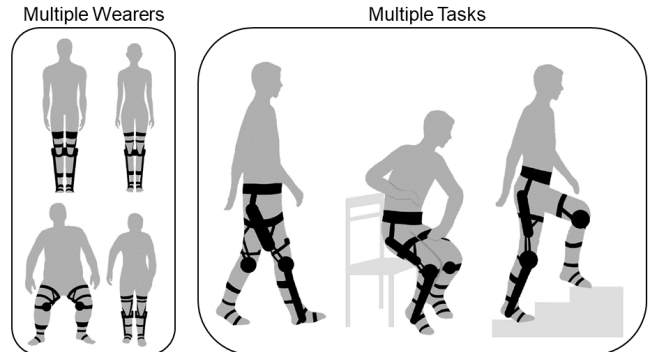


Fig. 1. The proposed method enables the lower-limb exoskeleton (in black) to provide individualized assistance for multiple wearers with different backgrounds (left) and in multiple tasks (right), e.g., walking, sit-to-stand, climbing stairs.

based on a given task and human motion intention. In contrast, rehabilitation-based exoskeletons may focus on providing specific resistance or assistance to promote effort, motor learning, and recovery.

In the literature, a range of control approaches have been reported, allowing the robot to provide empathetic assistance [7]. However, most of the current lower-limb exoskeletons are designed for a specific task (e.g., ground walking only) or personalized for individual users. When they are deployed for different tasks or users, manual programming or even fine-tuning is typically necessary to set the assistance strategy or reference trajectory. Although the tasks of lower-limb exoskeleton in rehabilitation training are well-defined and largely invariable, the demands are more diverse when assisting a healthy individual (Fig. 1), encompassing various tasks (e.g., walking, squatting, standing up, and climbing stairs), different wearers (with different walking speeds, patterns, or habits), and the appearance of anomalous events during the task (e.g., physical conflicts, fatigue, and imbalance). Therefore, the ability of online learning and adaptation to multiple tasks and wearers is important to ensure that the robot provides effective assistance in practical applications.

To fulfill these requirements, a novel human-in-the-loop (HIL) framework is established in this study to enhance the online learning and adaptation ability of lower-limb exoskeletons. The contributions of this work can be summarized as follows.

- An unsupervised detection network is constructed to address anomalies during the task. This network prevents the robot from learning or providing assistance based on

incorrect patterns without affecting its generalizability, while optimizing trajectory generation to minimize conflicts.

- An online individualizing approach is developed, using dynamic movement primitives (DMP) to parameterize the assistance trajectory and Bayesian optimization to minimize the cost function, enabling the provision of personalized assistance to multiple wearers.
- A neural network (NN) is trained to serve as the task translator. This allows optimized assistance for ground walking to be transferred to a variety of tasks may not be suitable for online learning, such as stair climbing.
- A unified variable impedance model is proposed to integrate the individualized and generalized trajectories. Moreover, a singular-perturbation approach is developed to implement the model with low-computation complexity without the need for force sensors.

The proposed framework relies solely on the proprioceptive sensors of exoskeleton robots (e.g., encoders and strain gauges), without external sensors (e.g., electroencephalographic/electromyographic (EMG) sensors or motion capture systems). Thus, it can be easily implemented, consistent with the practical scenarios of human assistance. All phases of optimization and inference are realized online, ensuring data efficiency without the need for pre-training. The stability of the compliantly-driven exoskeleton and convergence to the variable impedance model are theoretically grounded. A series of ablation studies and experiments are conducted on a lower-limb exoskeleton robot to illustrate the effectiveness of the developed framework in different tasks and for multiple wearers. In previous work [8], we developed a variable impedance controller to relax physical conflicts during the human-robot interaction by using proprioceptive sensors and a variational autoencoder (VAE) based detection network. In this study, we extend this controller to an anomaly-sensitive online adaptation framework, considering multiple tasks and individualization.

II. RELATED WORKS

The section provides an overview of research related to trajectory generation and interaction control for exoskeleton robots.

Trajectory Generation: This study focuses on the trajectory generation for exoskeletons designed to assist multiple wearers across different tasks.

One approach to achieving individualized assistance for multiple wearers is HIL optimization, where the body features and walking habits of the users are implicitly considered [9]. Leveraging sampling-based nonlinear optimization, a HIL optimization technique for an ankle exoskeleton was first proposed in [10], where the metabolic rate was reduced through a covariance matrix adaptation evolution strategy (CMA-ES). Further individualization was achieved through an intuitive gait parameter adjustment method named “Iterative Learning of Human Behavior (ILHB)”, which optimizes joint-reference trajectories based on observed ground contact timing

[11]. The HIL optimization concept has also been applied to wearable robots with multiple joints [12], prostheses [13], and soft exosuits [14]. In addition, reinforcement learning (RL) [15], impedance control [16], and a sampling-efficient method utilizing user preferences [17] have been integrated into the HIL optimization framework to offer timely and adaptive assistance. In parallel, various strategies have been proposed to decrease the optimization time. In [18], real-time regression technology is employed to expedite the estimation of steady-state metabolic rates within the HIL framework. In [19], the complexity of assistance variables is reduced by focusing solely on a stiffness parameter. Meanwhile, [20] utilizes the symmetric foot force-time integral as a substitute for estimated metabolic rates. Unlike these studies, which emphasized the reduction of the wearers' metabolic rate, this paper proposes a new cost function to realize both the assistance and wearer's comfort. Furthermore, instead of using multiple external sensors [21], [22], the proposed learning framework relies only on proprioceptive sensors (i.e., encoders on the robot) with better portability and practicability.

As the assistance profiles for different tasks vary significantly, multiple control algorithms have been designed for specific tasks, such as walking [11], ascending stairs [23], and addressing gait asymmetry [24]. In [25], the joint kinematics was simultaneously generalized for different walking speeds and slopes using interpolation techniques. Furthermore, kinematics of ascending stairs and transitional motion were predicted based on Bernstein basis polynomials in [26], promoting robustness in the lower-limb exoskeleton. However, these studies typically focused on a single task or task generalization under different configurations. To encompass multitask assistance, an open-sourced framework for wearable robots was established in [27] to incorporate various cost functions. The researchers in [28] developed a soft and flexible bioelectronic system and extended the assistive scenario to the squatting task. While the aforementioned frameworks could assist with multiple tasks, transferring optimized and individualized results across different tasks is challenging.

Interaction Control: The purpose of interaction control is to drive the exoskeleton robot along the generated trajectory while ensuring the safety of the wearer. Among different control schemes, variable impedance control (VIC) has been extensively implemented in various robotic systems involving physical interaction [29]. VIC is inspired by human behavior and biomechanics, wherein the central nervous system can continuously modulate the physical impedance of human limbs to adapt to uncertain environments, different types of tasks, and external perturbations [30]. In [31], VIC was deployed in a lower-limb rehabilitation exoskeleton. The deviation between the human intended motion and current joint angle of the exoskeleton was used to vary the impedance parameters to resolve physical conflict. In [32], VIC was applied to a collaborative assembly task, where the robot varied its stiffness based on the interaction with the human subject and the learned impedance behavior from demonstrations. Furthermore, the impedance parameters can be adjusted while considering other

variables, such as the velocity [33] and center of mass location [34].

Several learning-based approaches have also been developed to achieve interaction control. In [35], an inverse reinforcement learning-based method was designed for impedance learning, where the reward function associated with the trajectory tracking error and impedance switching policy for the action space were learned from expert demonstrations. In [36], a reinforcement learning policy was formulated by combining the output impedance and desired trajectory, and a reward term was designed to implement the learned variable impedance policy. In [37], dynamic movement primitives (DMP) were introduced to learn and reproduce the movement trajectory and stiffness profile learned from demonstrations. In [38], a Gaussian-mixture-model-based, state-dependent variable impedance method was proposed to transfer human impedance behavior to the robot while ensuring stability.

Despite significant advancements in VIC for exoskeleton robots, most of the existing control schemes cannot detect or alleviate physical conflicts, e.g., motion asynchronization, human fatigue, and imbalance during walking, resulting in potential safety issues.

III. PRELIMINARIES

The exoskeleton robot considered in this study is driven by series elastic actuators (SEAs), the principle of which is illustrated in Fig. 2. Unlike rigid actuators, an elastic element (e.g., a spring) is installed between the driving motor and robot joint, which can store excessive energy and tolerate impacts, thereby ensuring structural safety.

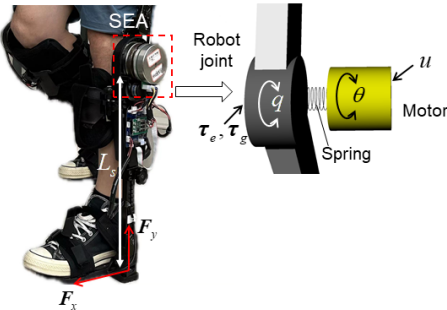


Fig. 2. An illustration of a lower-limb exoskeleton driven by series elastic actuators (SEAs), where a spring is installed between the driving motor and robot joint. Specifically, \mathbf{u} is the control input exerted by the motor, τ_e signifies the interaction torque, τ_g denotes the torque resulting from the ground reaction forces F_x, F_y , and L_s represents the length of the shank. Additionally, \mathbf{q} refers to the rotational angle of the robot joint, while θ indicates the rotation of the motor rotor.

We model each leg individually, and the dynamic model of a SEA-driven exoskeleton robot can be described as [39]

$$\mathbf{M}(\mathbf{q})\ddot{\mathbf{q}} + \mathbf{C}(\dot{\mathbf{q}}, \mathbf{q})\dot{\mathbf{q}} + \mathbf{g}(\mathbf{q}) = \mathbf{K}(\theta - \mathbf{q}) + \tau_e + \tau_g, \quad (1)$$

$$\mathbf{B}\ddot{\theta} + \mathbf{K}(\theta - \mathbf{q}) = \mathbf{u}, \quad (2)$$

where (1) and (2) describe the subsystems at the robot side and the actuator side, respectively, which are coupled with the output torque of the SEA, that is, $\tau_o = \mathbf{K}(\theta - \mathbf{q})$. Specifically, $\mathbf{q} \in \mathbb{R}^n$ denotes the vector of the joint angles of the robot; n is the number of degrees of freedom (DoFs); $\theta \in \mathbb{R}^n$ denotes the vector of the rotational angles of the rotors; $\mathbf{K} \in \mathbb{R}^{n \times n}$ is the stiffness matrix; $\mathbf{M}(\mathbf{q})$ and $\mathbf{B} \in \mathbb{R}^{n \times n}$ are the inertia matrices

for the robot and actuator, respectively; $\mathbf{C}(\dot{\mathbf{q}}, \mathbf{q}) \in \mathbb{R}^{n \times n}$ is a matrix related to the centripetal and Coriolis forces; $\mathbf{g}(\mathbf{q}) \in \mathbb{R}^n$ is a vector of gravitational torque; $\tau_e \in \mathbb{R}^n$ is a vector associated with physical interaction; $\tau_g \in \mathbb{R}^n$ is the torque vector resulted by the ground reaction forces, and $\mathbf{u} \in \mathbb{R}^n$ denotes the control input, which is also the torque exerted by the driving motor.

The dynamic model described by (1) and (2) exhibits the following properties [40], [41]:

- 1) The matrix $\mathbf{M}(\mathbf{q})$ is bounded, symmetric, and positive definite;
- 2) The term $\dot{\mathbf{M}}(\mathbf{q}) - 2\mathbf{C}(\mathbf{q}, \dot{\mathbf{q}})$ is skew-symmetric;
- 3) The matrices \mathbf{B} and \mathbf{K} are constant, diagonal, and positive definite.

We assume that the dynamic parameters (i.e., $\mathbf{M}(\mathbf{q})$, $\mathbf{C}(\dot{\mathbf{q}}, \mathbf{q})$, $\mathbf{g}(\mathbf{q})$, \mathbf{K} , \mathbf{B}) are known or can be obtained with sufficient accuracy from datasheets or using calibration and identification techniques [42].

The dynamic model of the overall system, described by (1) and (2), exhibits different time scales. Specifically, the SEA subsystem is slower, and the robot subsystem is faster. To control this system according to the singular perturbation theory [43], the control input can be designed as

$$\mathbf{u} = \mathbf{u}_f + \mathbf{u}_s, \quad (3)$$

where \mathbf{u}_f denotes the fast time-scale control term for stabilizing (2), and \mathbf{u}_s denotes the slow time-scale control term to stabilize (1). A representative \mathbf{u}_f can be expressed as

$$\mathbf{u}_f = -\mathbf{K}_v(\dot{\theta} - \dot{\mathbf{q}}), \quad (4)$$

where $\mathbf{K}_v \in \mathbb{R}^{n \times n}$ is a diagonal and positive-definite matrix.

Substituting (3) and (4) into (2) yields

$$\mathbf{B}\ddot{\theta} + \mathbf{K}(\theta - \mathbf{q}) + \mathbf{K}_v(\dot{\theta} - \dot{\mathbf{q}}) = \mathbf{u}_s, \quad (5)$$

which can be rewritten as

$$\mathbf{B}(\ddot{\theta} - \ddot{\mathbf{q}}) + \mathbf{K}(\theta - \mathbf{q}) + \mathbf{K}_v(\dot{\theta} - \dot{\mathbf{q}}) = \mathbf{u}_s - \mathbf{B}\ddot{\mathbf{q}}. \quad (6)$$

Note that $\tau_o = \mathbf{K}(\theta - \mathbf{q})$. By introducing $\mathbf{K} = \mathbf{K}_1/\varepsilon^2$ and $\mathbf{K}_v = \mathbf{K}_2/\varepsilon$, with ε being a small positive parameter, (6) can be written as

$$\varepsilon^2 \mathbf{B}\ddot{\tau}_o + \varepsilon \mathbf{K}_2 \dot{\tau}_o + \mathbf{K}_1 \tau_o = \mathbf{K}_1(\mathbf{u}_s - \mathbf{B}\ddot{\mathbf{q}}). \quad (7)$$

When $\varepsilon=0$, the solution of (7) is $\bar{\tau}_o = \mathbf{u}_s - \mathbf{B}\ddot{\mathbf{q}}$.

If the fast time-scale is set as $\gamma = \frac{t}{\varepsilon}$, $\bar{\tau}_o$ is achieved at $\gamma \rightarrow \infty$. Note that $\bar{\tau}_o$ remains constant at $\varepsilon=0$. Thus, a new variable is introduced as $\eta = \tau_o - \bar{\tau}_o$ to rewrite (7) on the fast time-scale:

$$\mathbf{B}\left(\frac{d^2\eta}{d\gamma^2}\right) + \mathbf{K}_2\left(\frac{d\eta}{d\gamma}\right) + \mathbf{K}_1\eta = 0, \quad (8)$$

which is referred to as the *boundary-layer system*.

Then, substituting this solution into (1), a *quasi-steady-state system* can be derived as

$$(\mathbf{M}(\mathbf{q}) + \mathbf{B})\ddot{\mathbf{q}} + \mathbf{C}(\dot{\mathbf{q}}, \mathbf{q})\dot{\mathbf{q}} + \mathbf{g}(\mathbf{q}) = \mathbf{u}_s + \tau_e. \quad (9)$$

According to the singular perturbation theory, the stability of the overall system is guaranteed if both the *boundary-layer*

system and the *quasi-steady-state system* are exponentially stable.

In addition, the control objective for (9) can be specified as

$$C_d(\dot{q} - \dot{q}_d) + K_d(q - q_d) = \tau_e, \quad (10)$$

which describes a first-order impedance model with the desired damping and stiffness matrices (i.e., $C_d, K_d \in \mathbb{R}^{n \times n}$), allowing the robot joint to deviate from the reference trajectory $q_d \in \mathbb{R}^n$, thereby ensuring safe interaction. Note that the desired inertia is neglected, matching the lower-limb model of human users [44]. In summary, the wearer's safety is ensured by both hardware (i.e., SEA) and software (e.g., impedance control) considerations in the proposed framework.

Objective: This paper aims to propose a new HIL framework with both variable impedance control and individualized trajectory generation for lower-limb exoskeleton actuated by SEAs, to provide effective assistance for different wearers in multiple tasks.

The overall framework is mainly constituted by three modules, i.e., offline learning, HIL optimization and variable impedance control, and hence it is organized under the section structure in the subsequent development. The relationship between sections is shown in Fig. 3. Specifically, Section IV presents the anomaly detection network and the task translator, which are used in Section V to generate the individualized trajectory for different human subjects and also shape it in multiple tasks, respectively. The generated and shaped trajectory is included in a variable impedance model in Section VI, whose parameters are varied according to the anomaly score, to regulate the exoskeleton robot's action to assist the subject.

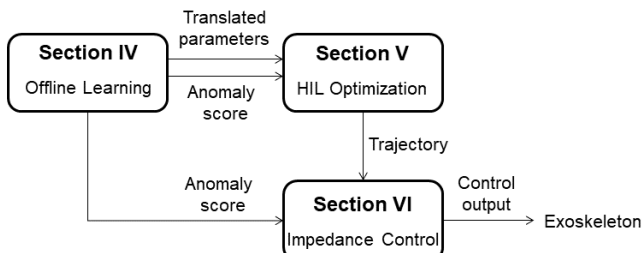


Fig. 3. The proposed framework is organized with three sections, i.e., Offline Learning, HIL Optimization, and Variable Impedance Control.

Remark 1: Note that the viscous friction is negligible because other dynamic effects, including the inertia and the output torque of SEA, are more dominant [45]. In the case that the viscous friction is not negligible, it can be approximated and then compensated for with learning-based techniques such as [46].

IV. OFFLINE LEARNING

The workflow of the proposed learning and control framework is shown in Fig. 4. The individualized trajectory is generated through the offline learning phase and then the HIL optimization. The trajectory is integrated into a variable impedance model, and the robot tracks this model to provide safe and effective assistance. Both HIL optimization and

impedance control operate simultaneously in the online phase. The proposed framework offers several advantages, including ease of implementation and adaptability to multiple tasks and human subjects:

- Only proprioceptive sensors, which are typically integrated into the exoskeleton, are required for trajectory learning and interaction control, resulting in cost effectiveness and reduced complexity;
- Using common sensors, the robot can effectively adapt to new users and tasks that are not included in the offline training;
- This adaptation process requires the data of only a few users to fit the nonlinear relationships between different patterns.

In the offline stage, multiple human subjects wear the exoskeleton to perform various tasks (e.g., walking on the ground or ascending stairs, etc.). The joint trajectories of the exoskeleton robot are recorded and represented as the joint motion of human subjects. During the collection of datasets, the robot works under the transparent mode [47] where the motors are powered to drive the robot to passively follow the wearer, thereby simulating his/her natural movements without the exoskeleton; in addition, the interaction force used in such a mode is estimated with the disturbance observer (DOB) such that additional force sensors are not required. The collected datasets are used to train anomaly detection and task translation modules. The anomaly detection module shapes the impedance parameter (with the weighting function) and guides HIL optimization, while task translation establishes the mappings among multiple tasks.

Anomaly Detection: During closely coupled interaction, a mismatch between the wearer and robot may result in physical conflict, which can adversely influence the assistance efficiency and safety. The proposed framework detects and then alleviates such conflicts.

The anomaly detection module is based on a VAE (Fig. 4). The VAE, receives two types of information from proprioceptive sensors (i.e., encoders and force sensors built into the exoskeleton): joint torques (based on spring deflection measurements) and joint positions (based on rotation angle measurements) and outputs a continuous anomaly score.

To handle time-series signals, a sliding window is introduced to segment the data, which is then input to the network. In the proposed network, latent variables are used to capture normal patterns of the input signals and then reconstruct the original data. The anomaly score is obtained by calculating the reconstruction error, which increases when the physical conflict is significant and decreases when the conflict is relaxed.

To train the proposed network, the latent variable ρ is re-parameterized as

$$\rho = \mu + \sigma \odot \epsilon, \quad (11)$$

where μ and σ are the mean and standard deviation obtained from the encoder, respectively. Sample noise is set to obey the standard normal distribution i.e., $\epsilon \sim \mathcal{N}(0, I)$.

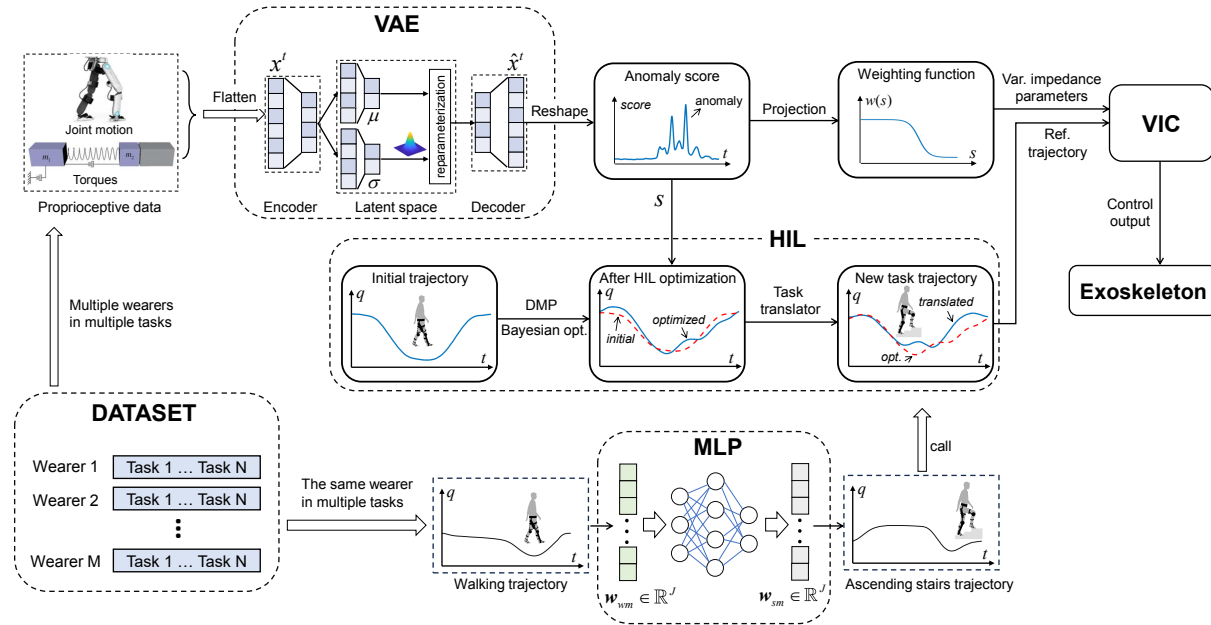


Fig. 4. Workflow of the proposed learning and control method, where M is the number of human users, N denotes the number of tasks, \mathbf{W}_{wm} and \mathbf{W}_{sm} denote the learned parameters from different tasks, s is the anomaly score. The collected **DATASET** is used to train anomaly detection (VAE) and task translation (MLP) modules. Both modules are used to generate the individualized trajectory for different wearers and also shape it in multiple tasks, respectively, during the **HIL** optimization. The generated and shaped trajectory is integrated into a variable impedance model (VIC), such that the exoskeleton robot tracks this model to provide safe and effective assistance.

The loss function can be formulated as

$$\mathcal{L}_{VAE}(\mathbf{x}^t) = \|\mathbf{x}^t - \hat{\mathbf{x}}^t\|^2 + KL[\mathcal{N}(\mu, \sigma), \mathcal{N}(0, \mathbf{I})], \quad (12)$$

which consists of both the reconstruction error and the Kullback–Leibler-divergence, with $\mathbf{x}^t, \hat{\mathbf{x}}^t \in \mathbb{R}^{L_s N_c}$ denoting the input to the encoder and the output from the decoder, respectively. Here, L_s denotes the width of the sliding window, and N_c refers to the number of data channels. In anomaly detection tasks, the reconstruction error of VAE is typically used to represent the anomaly score [48].

$$s = MSE(\mathbf{x}^t, \hat{\mathbf{x}}^t) = \|\mathbf{x}^t - \hat{\mathbf{x}}^t\|^2. \quad (13)$$

Training is performed by inputting the data of M human users, with N tasks for each user, into the constructed VAE. This anomaly detection model is trained in an unsupervised manner, and its output score represents the conflict among different wearers and tasks. The process for implementing anomaly detection is detailed in the appendix.

Task Translation: All collected datasets are used to train the task translator module, to uncover the relationships among multiple tasks. The proposed task translator is based on a Multi-Layer Perceptron (MLP). Unlike VAE-based training, each entry fed into the task translator represents parameterized trajectories (i.e., weight matrices) for various tasks performed by a single user. Details of the trajectory encoding are presented in Section V. The identified relationships allow the robot to transfer learned tasks to new ones in the subsequent online HIL phase. These tasks are typically not repeatable (e.g., ascending stairs and standing up) and thus impractical for online learning.

Fig. 4 illustrates the workflow of task translation, wherein \mathbf{w}_{wm} and \mathbf{w}_{sm} represent the encoded weight vector associated with a single joint, specifically the knee joint, for user m

during the tasks of walking and ascending stairs, respectively. These vectors are processed through DMP, as discussed in Section V. To train the task translator, gait trajectories in the different tasks are collected in weight matrix form as a training set $(\mathbf{W}_{wm}, \mathbf{W}_{sm})$, where \mathbf{W}_{wm} and \mathbf{W}_{sm} are the weight matrices that stack the weight vectors of multiple joints for user m during the tasks of walking and ascending stairs, respectively. Then, the MLP is used to determine the mapping relationship of the weight matrices under different tasks. The predictive weight matrix in the new task is obtained as

$$\hat{\mathbf{W}}_{sm} = \mathbf{F}_r(\mathbf{W}_{wm}), \quad (14)$$

where \mathbf{F}_r is a nonlinear regression function yielded by a neural network.

The following loss function is minimized

$$\mathcal{L} = \sum_m l(\mathbf{W}_{sm}, \hat{\mathbf{W}}_{sm}), \quad (15)$$

where l is a differentiable convex loss function that represents the distance between the prediction $\hat{\mathbf{W}}_{sm}$ and target \mathbf{W}_{sm} , and M is the number of users. Function l is written in the following quadratic form:

$$l(\mathbf{W}, \hat{\mathbf{W}}) = \|\mathbf{W} - \hat{\mathbf{W}}\|_F^2, \quad (16)$$

where $\|\cdot\|_F$ indicates the Frobenius norm.

Compared with techniques commonly used for prediction, such as K-Nearest Neighbors (KNN), Gaussian Process Regression (GPR), Extreme Gradient Boosting (XGBoost), Gradient Boosting (GBoost), and Support Vector Machines (SVM), the proposed NN-based task translator exhibits better generalization performance over a limited dataset, as validated experimentally.

Notably, user-specific body parameters, such as height and upper limb arm length, relevant to the optimization process

[3] and related to gait trajectory, are implicitly incorporated within the weight matrix. For trajectory recording, the proposed task translator requires only proprioceptive sensors.

Remark 2: There are frameworks where the exoskeleton robot employs other sensors (instead of proprioceptive ones only) to perceive the wearer's response or the environmental changes [21], [22], [49]. While using other external sensors does provide richer information about the wearer and the environment from different perspectives, it usually needs additional installation and also re-calibration every time a new task is given. Unlike the aforementioned studies, the proposed framework with proprioceptive sensors only has the advantages of relatively low cost, ease of implementation, and fast deployment for multiple wearers and tasks.

Remark 3: The measure of conflict within this study is defined in relation to the dataset collected (the same as other applications [48], [50]). There might exist instances where certain data points diverge from the training data, yet these deviations are, in fact, normal occurrences when the subject undertakes tasks not encompassed in the dataset, such as walking on different slopes. To address this issue, unseen but normal motion data for additional tasks can be collected and added to train the VAE. Then, even if similar data point deviations occur, they are not flagged as conflicts.

Remark 4: Compared with a single MSE setting or several independent models, using the VAE for conflict detection has several advantages. First, it can receive multi-modal data and explore their underlying relationship in latent space to describe the conflict without establishing an explicit model and hence achieve more accurate detection. Second, the VAE can generate probabilistic models, which can effectively express the uncertainties of wearers.

V. HIL OPTIMIZATION

This section presents a new HIL optimization scheme for exoskeleton robots to facilitate their online adaptation to different wearers (with various walking habits and body parameters) across multiple tasks. This adaptability is important for robots to exhibit operational flexibility in real-world applications.

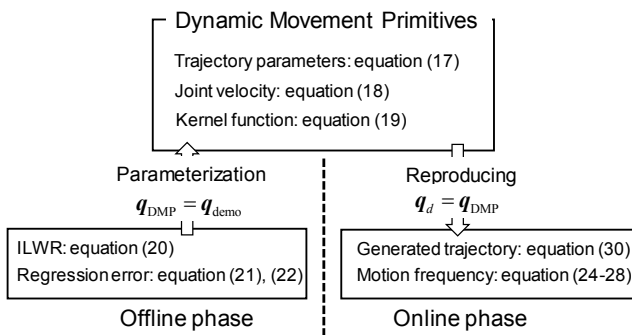


Fig. 5. Under the DMP formulation, the trajectory parameters are first initiated in the offline phase with the dataset, and then the parameters are updated in the online phase to generate the individualized trajectory.

The joint trajectory of the exoskeleton robot is modeled with the approach of DMP [51], which basically encodes the trajectory via an *output system* as:

$$\dot{\omega}_i = -2\pi \left[\alpha_o(\beta_o \cdot q_{DMP,i} + \omega_i) + \frac{\sum_{j=1}^J \Psi_j w_{ij}}{\sum_{j=1}^J \Psi_j} \right], \quad (17)$$

$$\dot{q}_{DMP,i} = 2\pi \cdot \omega_i, \quad (18)$$

$$\Psi_j = \exp[h(\cos(2\pi \cdot t - c_j) - 1)], \quad (19)$$

where $q_{DMP,i}$ and ω_i correspond to the normalized joint angle and velocity, respectively, for the i -th joint. The parameters α_o and β_o are positive constants. The term w_{ij} represents the weights of the i -th joint to be updated which can be treated as the trajectory parameters, and Ψ_j represent Gaussian-like kernel functions with a width h and center c_j . In practice, after determining the number of kernels J , h is typically set as $2.5J$ and c_j is evenly spaced in $[0, 2\pi]$. Under such formulation, the trajectory parameters are first initiated in the offline phase with the dataset, and then the parameters are updated in the online phase to generate the desired trajectory, as seen in Fig. 5.

Trajectory Parameterization: Given that the dataset records a series of joint trajectories for multiple wearers in multiple tasks, the mean trajectory is selected for demonstration and denoted as the vector q_{demo} . In the offline phase, the trajectory parameters are initialized by setting them as $q_{DMP} = q_{demo}$, where $q_{DMP} = [q_{DMP,1}, \dots, q_{DMP,i}, \dots, q_{DMP,n}] \in \mathbb{R}^n$, and then the parameters (i.e., the weighting matrix) are learned through Incremental Locally Weighted Regression (ILWR) [52] as

$$w_{ij}(t+1) = w_{ij}(t) + \Psi_j Q_{ij}(t+1) e_{r,ij}(t), \quad (20)$$

$$Q_{ij}(t+1) = \frac{1}{\Lambda} \left(Q_{ij}(t) - \frac{Q_{ij}(t)^2}{\Psi_j} \right), \quad (21)$$

$$e_{r,ij}(t) = \frac{1}{(2\pi)^2} \ddot{q}_{demo,i} + \alpha_o (\beta_o \cdot q_{demo,i} + \frac{1}{2\pi} \dot{q}_{demo,i}) - w_{ij}(t), \quad (22)$$

where Λ denotes a forgetting factor, and Q_{ij} and $e_{r,ij}$ denote the auxiliary variable and regression error, respectively, with $q_{demo,i}$ being the demonstration on joint i (i.e., the i -th element of the vector q_{demo}). ILWR learning weights offer advantages of high computational efficiency, avoiding overfitting, and mitigating the impact of noisy data. The method of trajectory encoding using DMP has already been open-sourced¹.

Trajectory Generation: In the online phase, the trajectory parameters are updated with the proposed HIL method (which is to be detailed later) and now the desired trajectory can be computed in a forward manner as

$$q_{DMP} = f_p(t, \mathbf{W}, \Omega_c), \quad (23)$$

where Ω_c is the gait frequency, \mathbf{W} is the weight matrix with elements w_{ij} , where each row of \mathbf{W} corresponds to the weights associated with a single joint, and f_p is the function that integrates the *output system* with a subsequent integral

¹https://github.com/STAN-32/HIL_BO_with_DMP_encoder

process. To determine the frequency Ω_c , another *canonical system* is implemented as

$$\dot{\phi}_{ij} = j\Omega_i - k_{c1}e_i \sin(\phi_{ij}), \quad (24)$$

$$\dot{\Omega}_i = -k_{c1}e_i \sin(\phi_{i1}), \quad (25)$$

$$\tilde{q}_i = \sum_j A_{ij} \cos(\phi_{ij}), \quad (26)$$

$$\dot{A}_{ij} = k_{c2}e_i \cos(\phi_{ij}), \quad (27)$$

$$e_i = q_i - \tilde{q}_i, \quad (28)$$

where q_i is the current state of the i -th joint, obtained using encoders installed to the joints of the robot. The terms \tilde{q}_i and e_i are defined as the auxiliary state and the learning error for joint i , respectively. ϕ_{ij} and A_{ij} represent the phase and amplitude of the j -th component in the i -th joint, respectively, and k_{c1} and k_{c2} are positive constants. Then, we have

$$\Omega_c = \frac{1}{N_a} \sum_i^{N_a} \Omega_i, \quad (29)$$

where N_a is the number of the active joints. Note that the gait frequency is computed by detecting the discrete events of heel strikes with the strain gauge at the footplate.

Now, the desired trajectory can be specified as $q_d = q_{\text{DMP}}$. Note that discrete movements [51], such as sitting and standing, can also be represented using DMP within a unified framework by encoding them as a weight matrix \mathbf{W} . In addition, as the time required to perform the movement does not vary significantly across individuals, speed modulation is not required. Therefore, the generated trajectory can be expressed as

$$q_d = \begin{cases} f_p(t, \mathbf{W}, \Omega_c), & \text{periodic movement} \\ f_d(t, \mathbf{W}), & \text{discrete movement} \end{cases} \quad (30)$$

where $f_d(t, \mathbf{W})$ is the second-order dynamic system under discrete movement conditions.

Next, the generated trajectory is optimized under the HIL framework. Specifically, a comprehensive cost function is formulated using both the parameterized trajectory and anomaly score as

$$\mathcal{J}_{\text{HIL}}(s, q, \mathbf{W}) = \frac{\lambda}{T} \sum_i^{N_a} \sum_j^T (q_{di}^{(j)} - q_i^{(j)})^2 + \frac{1-\lambda}{T} \sum_j^T s^{(j)}, \quad (31)$$

where the superscript and subscript indicate the time index and joint index in a gait cycle, respectively. Furthermore, T represents the duration of one gait cycle. The first term ensures that the generated trajectory matches the specific user, and the second term helps ignore the abnormal patterns of the user (likely attributable to physical conflicts) during the learning process. The weight of these two terms is governed by the hyper-parameter $\lambda \in (0, 1)$. Specifically, when $\lambda = 0$, optimization is based on only the collected dataset. Conversely, when $\lambda = 1$, the emphasis shifts to optimizing the trajectory alignment.

Bayesian optimization is applied to determine the global minimum of $\mathcal{J}_{\text{HIL}}(s, q, \mathbf{W})$ under a bounded feasible set, which has proven effective in previous HIL protocols [53]. To this end, the selected matrices and their associated costs are

collated into $\mathcal{W}_{\text{past}}$ and $\mathcal{J}_{\text{past}}$ respectively. Note that $\mathcal{J}_{\text{past}}$ is formulated as a vector. Subsequently, we model the target function using Gaussian processes as

$$\begin{bmatrix} \mathcal{J}_{\text{new}} \\ \mathcal{J}_{\text{past}} \end{bmatrix} \sim \mathcal{N} \left(\mathbf{0}, \begin{bmatrix} K_{nn} & \mathbf{K}_{pn}^T \\ \mathbf{K}_{pn} & \mathbf{K}_{pp} \end{bmatrix} \right), \quad (32)$$

where \mathcal{J}_{new} represents the cost corresponding to the weight matrix \mathbf{W}^{new} to be identified. Notably, setting the mean as zero simplifies the calculation, which has proven effective in practice [53] as most of the information is contained in the covariance. Using the radial basis function as the kernel function, $k(\mathbf{x}, \mathbf{x}')$, we introduce kernel matrices K_{nn} , \mathbf{K}_{pn} , and \mathbf{K}_{pp} with the following elements:

$$K_{nn} = k(\text{Vec}(\mathbf{W}^{\text{new}}), \text{Vec}(\mathbf{W}^{\text{new}})), \quad (33)$$

$$K_{in} = k(\text{Vec}(\mathbf{W}_i), \text{Vec}(\mathbf{W}^{\text{new}})), \quad \mathbf{W}_i \in \mathcal{W}_{\text{past}} \quad (34)$$

$$K_{ij} = k(\text{Vec}(\mathbf{W}_i), \text{Vec}(\mathbf{W}_j)). \quad \mathbf{W}_i, \mathbf{W}_j \in \mathcal{W}_{\text{past}} \quad (35)$$

Here, $\text{Vec}(\cdot)$ denotes a vectorization function. Following the construction of the posterior distribution, we use the Lower Confidence Bound (LCB) as the acquisition function for guiding the selection of the subsequent point for exploration:

$$\mathbf{W}^{\text{new}} = \underset{\mathbf{W}^{\text{new}}}{\operatorname{argmin}} \mu_{\text{new}} - v\sigma_{\text{new}}, \quad (36)$$

$$\mu_{\text{new}} = \mathbf{K}_{pn}^T \mathbf{K}_{pp}^{-1} \mathcal{J}_{\text{past}}, \quad (37)$$

$$\sigma_{\text{new}} = K_{nn} - \mathbf{K}_{pn}^T \mathbf{K}_{pp}^{-1} \mathbf{K}_{pn}, \quad (38)$$

where v is a positive hyperparameter. The minimization of (36) is implemented using the L-BFGS algorithm. This process enables iterative updates of the posterior distribution based on historical data, and the appropriate weight matrix is then derived from the acquisition function. To accelerate the convergence over the extended dimensions compared with previous research, the initial parameters are specified based on the sampled gait. Subsequently, the optimal weight matrix \mathbf{W}^* for the walking task can be learned based on the proposed cost function. Additionally, the methodology for conducting the optimization is now publicly available.

Minimizing (31) can yield an individualized and anomaly-robust trajectory (i.e., q_d), allowing the robot to learn the correct and appropriate gait trajectory under all conditions to improve the effectiveness of assistance and the wearer's comfort.

After the walking optimization \mathbf{W}_{wm}^* for user m is obtained, the optimal weight matrix for a new task can be predicted using the proposed task translator as

$$\hat{\mathbf{W}}_{sm}^* = \mathbf{F}_r(\mathbf{W}_{wm}^*), \quad (39)$$

which enables the provision of predictive assistance $\hat{\mathbf{W}}_{sm}^*$ without the demonstration of a new task based on the known optimization result. Thus, the proposed HIL optimization framework can effectively adapt to multiple wearers and tasks. The process for individualized trajectory generation is detailed in the appendix.

VI. VARIABLE IMPEDANCE CONTROL

The individualized and generalized trajectory is embedded into a variable impedance model to regulate the robot's action to provide safe and effective assistance. The impedance model is varied according to the anomaly score presented in Section IV to alleviate physical conflicts with the wearer. We consider the following aspects:

- When the anomaly score oscillates around a small value, the robot should ignore such minor conflicts to avoid over-reaction;
- When the anomaly score exceeds a certain threshold, significant conflicts may arise, which must be promptly addressed by the robot.

To this end, the anomaly score is transformed into a weighting function shown in Fig. 4, which is defined as

$$w(s) = \lambda_1 \tanh\left(-\frac{s}{\chi_1} + \chi_2\right) + \lambda_2, \quad (40)$$

where λ_1 and λ_2 are positive constants that determine the range and median of the weighting function, respectively; χ_1 is a constant that normalizes the anomaly score into a specified small range; and χ_2 represents the offset of the weighting function from the origin of the coordinates along the positive horizontal axis.

Next, the desired impedance model (10) is reformulated with the weighting function as

$$\mathbf{C}_d(\dot{\mathbf{q}} - \dot{\mathbf{q}}_d) + \mathbf{K}_d(\mathbf{q} - \mathbf{q}_d) = \frac{1}{w(s)}\boldsymbol{\tau}_e. \quad (41)$$

Multiplying both sides of (41) with $w(s)$ yields

$$\mathbf{C}_a(t)(\dot{\mathbf{q}} - \dot{\mathbf{q}}_d) + \mathbf{K}_a(t)(\mathbf{q} - \mathbf{q}_d) = \boldsymbol{\tau}_e, \quad (42)$$

where $\mathbf{C}_a(t) \triangleq w(s)\mathbf{C}_d$ and $\mathbf{K}_a(t) \triangleq w(s)\mathbf{K}_d$, varying according to the weighting function. Specifically, when the anomaly score increases, $w(s)$ is reduced, thus lowering the impedance parameters and ensuring that the robot reacts passively to the conflict. Otherwise, the impedance parameters return to their original values to maintain the assistance.

Then, an impedance vector is introduced as

$$\begin{aligned} \mathbf{z} &= \dot{\mathbf{q}} - \dot{\mathbf{q}}_r \\ &= \dot{\mathbf{q}} - \dot{\mathbf{q}}_d + \mathbf{C}_d^{-1}\mathbf{K}_d(\mathbf{q} - \mathbf{q}_d) - \frac{1}{w(s)}\mathbf{C}_d^{-1}\boldsymbol{\tau}_e, \end{aligned} \quad (43)$$

where

$$\dot{\mathbf{q}}_r = \dot{\mathbf{q}}_d - \mathbf{C}_d^{-1}\mathbf{K}_d(\mathbf{q} - \mathbf{q}_d) + \frac{1}{w(s)}\mathbf{C}_d^{-1}\boldsymbol{\tau}_e \quad (44)$$

is a reference vector. According to (43), the convergence of $\mathbf{z} \rightarrow \mathbf{0}$ implies the realization of the desired impedance model (41).

Notably, the impedance vector (43) depends on the interaction torque $\boldsymbol{\tau}_e$. To eliminate the use of sensors for torque measurement, a model-based disturbance observer (DOB) [54] is established to estimate the interaction torque:

$$\begin{cases} \dot{\mathbf{y}} = -\mathbf{L}(\dot{\mathbf{q}}, \mathbf{q})\mathbf{y} - \mathbf{L}(\dot{\mathbf{q}}, \mathbf{q})[\mathbf{K}(\theta - \mathbf{q}) \\ \quad - \mathbf{C}(\dot{\mathbf{q}}, \mathbf{q})\dot{\mathbf{q}} - \mathbf{g}(\mathbf{q}) + \mathbf{p}(\dot{\mathbf{q}}, \mathbf{q})], \\ \hat{\boldsymbol{\tau}}_e = \mathbf{y} + \mathbf{p}(\dot{\mathbf{q}}, \mathbf{q}), \end{cases}, \quad (45)$$

where $\hat{\boldsymbol{\tau}}_e \in \mathbb{R}^n$ denotes the estimated interaction torque, and $\mathbf{y} \in \mathbb{R}^n$ is an auxiliary vector used to make the observer independent of acceleration information.

According to [55], the observer gain matrix $\mathbf{L}(\dot{\mathbf{q}}, \mathbf{q}) \in \mathbb{R}^{n \times n}$ and vector $\mathbf{p}(\dot{\mathbf{q}}, \mathbf{q}) \in \mathbb{R}^n$ can be expressed as

$$\begin{cases} \mathbf{L}(\mathbf{q}, \dot{\mathbf{q}}) = \mathbf{A}^{-1}\mathbf{M}^{-1}(\mathbf{q}) \\ \mathbf{p}(\dot{\mathbf{q}}, \mathbf{q}) = \mathbf{A}^{-1}\dot{\mathbf{q}} \end{cases} \quad (46)$$

where $\mathbf{A} \in \mathbb{R}^{n \times n}$ denotes a constant and invertible matrix to be determined.

With the definition of the observation error as $\tilde{\boldsymbol{\tau}}_e = \hat{\boldsymbol{\tau}}_e - \boldsymbol{\tau}_e$, the closed-loop equation of the DOB can be given as

$$\dot{\tilde{\boldsymbol{\tau}}}_e = -\mathbf{L}(\mathbf{q}, \dot{\mathbf{q}})\tilde{\boldsymbol{\tau}}_e - \dot{\boldsymbol{\tau}}_e. \quad (47)$$

The following proposition can be derived to guarantee the convergence of $\tilde{\boldsymbol{\tau}}_e$.

Proposition 1: In the presence of $\|\dot{\boldsymbol{\tau}}_e\| \leq \zeta$ where ζ denotes the bound, the disturbance tracking error $\tilde{\boldsymbol{\tau}}_e$ is globally uniformly ultimately bounded, when \mathbf{A} is chosen such that the following condition is satisfied

$$\mathbf{A} + \mathbf{A}^T - \mathbf{A}^T \dot{\mathbf{M}}(\mathbf{q})\mathbf{A} = \boldsymbol{\Gamma} > \mathbf{0}, \quad (48)$$

where $\boldsymbol{\Gamma}$ is a positive definite matrix.

Proof: Consider the following candidate Lyapunov function:

$$V_e = \tilde{\boldsymbol{\tau}}_e^T \mathbf{A}^T \mathbf{M}(\mathbf{q}) \mathbf{A} \tilde{\boldsymbol{\tau}}_e. \quad (49)$$

Differentiating V_e with respect to time and substituting (47) into the expression yields

$$\begin{aligned} \dot{V}_e &= -\tilde{\boldsymbol{\tau}}_e^T (\mathbf{A} + \mathbf{A}^T - \mathbf{A}^T \dot{\mathbf{M}}(\mathbf{q})\mathbf{A}) \tilde{\boldsymbol{\tau}}_e \\ &\quad + \tilde{\boldsymbol{\tau}}_e^T \mathbf{A}^T \mathbf{M}(\mathbf{q}) \mathbf{A} \tilde{\boldsymbol{\tau}}_e + \tilde{\boldsymbol{\tau}}_e^T \mathbf{A}^T \mathbf{M}(\mathbf{q}) \mathbf{A} \dot{\boldsymbol{\tau}}_e. \end{aligned} \quad (50)$$

According to Schwartz inequality and the boundedness of $\|\dot{\boldsymbol{\tau}}_e\|$, it can be deduced that

$$\begin{aligned} \dot{V}_e &\leq -\lambda_{\min}(\boldsymbol{\Gamma})\|\tilde{\boldsymbol{\tau}}_e\|^2 + 2\zeta\lambda_{\max}(\mathbf{M}(\mathbf{q}))\|\mathbf{A}\|^2\|\tilde{\boldsymbol{\tau}}_e\| \\ &= -(1-\varrho)\lambda_{\min}(\boldsymbol{\Gamma})\|\tilde{\boldsymbol{\tau}}_e\|^2 - \varrho\lambda_{\min}(\boldsymbol{\Gamma})\|\tilde{\boldsymbol{\tau}}_e\|^2 \\ &\quad + 2\zeta\lambda_{\max}(\mathbf{M}(\mathbf{q}))\|\mathbf{A}\|^2\|\tilde{\boldsymbol{\tau}}_e\|, \end{aligned} \quad (51)$$

where $\varrho \in (0, 1)$.

Because $V_e \leq \lambda_{\max}(\mathbf{M}(\mathbf{q}))\|\mathbf{A}\|^2\|\tilde{\boldsymbol{\tau}}_e\|^2$, the inequality of

$$\dot{V}_e \leq -\frac{(1-\varrho)\lambda_{\min}(\boldsymbol{\Gamma})}{\lambda_{\max}(\mathbf{M}(\mathbf{q}))\|\mathbf{A}\|^2} V_e \quad (52)$$

is obtained if

$$\|\tilde{\boldsymbol{\tau}}_e\| \geq \frac{2\zeta\lambda_{\max}(\mathbf{M}(\mathbf{q}))\|\mathbf{A}\|^2}{\varrho\lambda_{\min}(\boldsymbol{\Gamma})}. \quad (53)$$

When (53) is satisfied, the last two terms of (51) are positive, and thus, inequality (52) is guaranteed.

Therefore, $\tilde{\boldsymbol{\tau}}_e$ converges asymptotically to the ball with radius $2\zeta\lambda_{\max}(\mathbf{M}(\mathbf{q}))\|\mathbf{A}\|^2/\varrho\lambda_{\min}(\boldsymbol{\Gamma})$ [41]. ■

The analytical solution of matrix \mathbf{A} can be expressed as [55]

$$\begin{aligned} \mathbf{A}^{-1} &= \frac{1}{2}(\sigma_1 + 2\beta\sigma_2)\mathbf{I}, \\ \|\dot{\mathbf{M}}(\mathbf{q})\| &\leq \sigma_1, \|\mathbf{M}(\mathbf{q})\| \leq \sigma_2, \end{aligned} \quad (54)$$

where β is a positive constant related to the convergence rate.

As mentioned in Section III, the overall control input is designed as (3), with the fast time-scale control term defined as in (4). Next, using the estimated interaction torque $\hat{\tau}_e$, the slow time-scale control term is established to stabilize (1) and achieve the desired impedance model as

$$\begin{aligned} \mathbf{u}_s = & -\mathbf{K}_z \mathbf{z} - \hat{\tau}_e - k_g \cdot \text{sgn}(\mathbf{z}) \\ & + (\mathbf{M}(\mathbf{q}) + \mathbf{B}) \ddot{\mathbf{q}}_r + \mathbf{C}(\dot{\mathbf{q}}, \mathbf{q}) \dot{\mathbf{q}}_r + \mathbf{g}(\mathbf{q}), \end{aligned} \quad (55)$$

where $\text{sgn}(\cdot)$ is the sign function defined as

$$\text{sgn}(z) = \begin{cases} 1, & z > 0 \\ 0, & z = 0 \\ -1, & z < 0 \end{cases} \quad (56)$$

where k_g is a positive constant, and $\mathbf{K}_z \in \mathbb{R}^{n \times n}$ is a diagonal and positive-definite matrix.

The stability of the overall system is guaranteed if both the boundary-layer system and quasi-steady-state system are exponentially stable. The following theorem can be stated:

Theorem 1: *The proposed controller \mathbf{u} in (3) guarantees the stability of the overall system if \mathbf{K}_1 and \mathbf{K}_2 are positive definite and k_g is adequately large.*

Proof: First, the exponential stability of the boundary-layer system in (8) can be guaranteed by appropriately tuning \mathbf{K}_1 and \mathbf{K}_2 .

Then, substituting (43) and (55) into (9) yields

$$(\mathbf{M}(\mathbf{q}) + \mathbf{B}) \dot{\mathbf{z}} + \mathbf{C}(\dot{\mathbf{q}}, \mathbf{q}) \mathbf{z} = -\mathbf{K}_z \mathbf{z} - \tilde{\tau}_e - k_g \text{sgn}(\mathbf{z}). \quad (57)$$

Next, a Lyapunov-like candidate is proposed as

$$V = \frac{1}{2} \mathbf{z}^T (\mathbf{M}(\mathbf{q}) + \mathbf{B}) \mathbf{z}. \quad (58)$$

Differentiating (58) with respect to time and substituting (57) into it yields the following expression:

$$\dot{V} = -\mathbf{z}^T \mathbf{K}_z \mathbf{z} - \mathbf{z}^T \tilde{\tau}_e - k_g \mathbf{z}^T \text{sgn}(\mathbf{z}). \quad (59)$$

As shown in **Proposition 1**, when $\|\dot{\tau}_e\| \leq \zeta$, the observation error is also bounded, and

$$\dot{V} \leq -\mathbf{z}^T \mathbf{K}_z \mathbf{z} - (k_g - \kappa) \|\mathbf{z}\|, \quad (60)$$

where

$$\kappa \geq \frac{2\zeta \lambda_{\max}(\mathbf{M}(\mathbf{q})) \|\mathbf{A}\|^2}{\varrho \lambda_{\min}(\mathbf{T})}$$

is a constant, representing the bound of the observation error.

If k_g is adequately large such that $k_g > \kappa$, we have

$$\dot{V} \leq -\mathbf{z}^T \mathbf{K}_z \mathbf{z} < 0, \quad (61)$$

As $V > 0$ and $\dot{V} < 0$, the *quasi-steady-state system* is also exponentially stable. According to Tikhonov's theorem [56], the stability of the closed-loop system is guaranteed, and convergence to the impedance vector is ensured. ■

VII. EXPERIMENT

The proposed scheme was implemented in a bilateral lower-limb exoskeleton robot to assess its performance, as shown in Fig. 6. All four joints of the robot, comprising two hip joints and two knee joints, were actuated by SEAs, with each leg having a weight of 6 kg. The spring stiffness of each SEA was 635 Nm, and the output torque was determined based on the spring deflection (measured using encoders) and known stiffness. The robot was equipped with two types of proprioceptive sensors: strain gauges and encoders (with 2048 lines). These sensors provided comprehensive task-specific information, including gait phases (measured using strain gauges), interaction torque, and movement trajectory (measured using encoders). During the experiment, four wireless surface EMG sensors (Ws450, Biometrics Ltd.) were mounted on human leg muscles, specifically, the quadriceps femoris (QF) and tibialis anterior muscle (TA) of the left and right legs, to collect the feedback of human limb and hence assess the performance of the proposed controller.

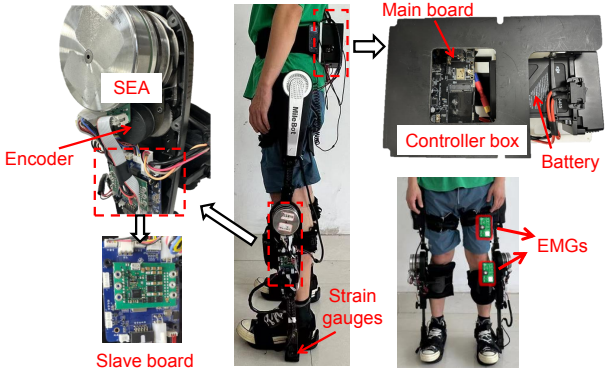


Fig. 6. Experimental setup of the exoskeleton robot, where all four joints of both legs are driven by the SEAs. The controller box is composed of the main board and battery. The commands are transmitted to four slave boards to drive the robot joints.

The control algorithm was programmed and realized by the main board, as shown in Fig. 6. The main board transmitted the control commands through the pulse width modulation (PWM) signals to the four slave boards to drive the motion of the four robot joints. The command frequency of the main board for sending control commands and PWM signals is set at 1 kHz, while the control frequency of the slave board operates at 4 kHz. Furthermore, owing to the constraints imposed by the hip joint components on the wearer's body shape and in order to reduce variable dimensions in optimization, only the two motors located at the knee joint were activated in this experiment.

Note that the dynamic parameters of the exoskeleton are obtained based on the open-source Orococos Kinematics and Dynamics Library (KDL)². Specifically, first, the exoskeleton is disassembled into a series of links and joints to construct the robot model, which defines the physical structure of the robot, including attributes such as the length, mass, and inertia of each link; then, the forward dynamics are calculated using Newton-Euler equations, by referring to that model. This paper considers the bilateral lower-limb exoskeleton with

²<https://www.orocos.org/wiki/orocos/kdl-wiki.html>

knee-joint actuation, and its dynamic model, derived from the general form, can be further described according to its specific structure and configuration:

- 1) The hip joints are modeled as loads to the knee-joint motors;
- 2) The lower leg is almost always vertical, as the angle between the lower leg and the vertical line is small during the standing phase and most of the swing phase;
- 3) Given the relatively slow walking speed, the inertial effect caused by the base movement can be omitted.

Then, the corresponding dynamic parameters can be specified in Table I.

TABLE I
DYNAMIC PARAMETERS IN THE EXPERIMENT

Parameter	Value
$M(q)$ ($\text{kg} \cdot \text{m}^2$)	3.12×10^{-2}
$C(\dot{q}, q)$ ($\text{kg} \cdot \text{m}^2/\text{s}$)	0
$g(q)$ ($\text{N} \cdot \text{m}$)	$2.2 \cdot \sin(q)$
K ($\text{N} \cdot \text{m}$)	635
B ($\text{kg} \cdot \text{m}^2$)	3.17×10^{-4}

In addition, since the dynamic model is dependent on the gait state, the gait state is taken into account within the KDL framework, where it is integrated with the position and velocity feedback and utilized for the computation of dynamics.

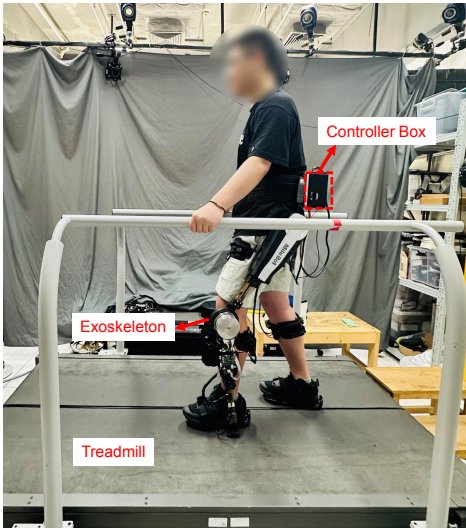


Fig. 7. Experimental setup for HIL optimization, where the participant walks on a treadmill with the exoskeleton.

Here are the experiments included in the following section:

- **Anomaly Detector:** This experiment aimed to assess the performance of our anomaly detection network. A participant intentionally held the robot to simulate conflict scenarios or adopted varied gait patterns to mimic balance loss due to fatigue. In addition, ablation studies were performed to show that the use of the force information provided by the SEA structure could enhance the detection accuracy compared with that associated with single sensory input.
- **Task Translator:** A comparative study was conducted to evaluate the accuracy of the proposed task translator in translating multiple various tasks.
- **HIL Optimization:** This experiment was to validate the feasibility of online optimization, specifically, on two

new participants who were not included in the pre-collected dataset. The participants were instructed to walk at a comfortable pace on a treadmill (FIT, Botic, USA), and the frequency of reference trajectory was set to a constant according to (29). This speed remained constant during the optimization process, as depicted in Fig. 7.

- **Translated Assistance:** In this experiment, the translated trajectory was implemented in the exoskeleton, and participants were instructed to wear the lower-limb exoskeleton and perform various tasks with different types of assistance. Importantly, participants were unaware of the specific type of assistance being provided during the experiment.

The experimental schedule for those required to continuously wear the lower limb exoskeletons is illustrated in Fig. 8.

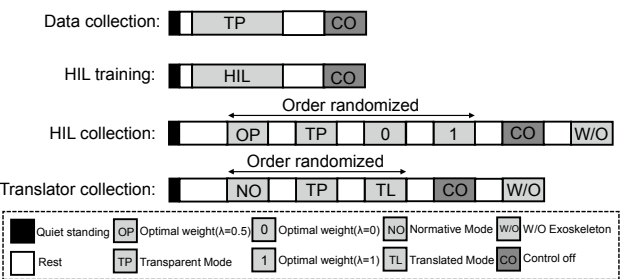


Fig. 8. A structured schedule for data collection, HIL training, data collection for HIL evaluation, and data collection for evaluation under the translation to new tasks.

Ten able-bodied participants with no prior experience with exoskeletons performed multiple tasks while wearing the exoskeleton. Table II presents an overview of the participants' statistical attributes, namely age (25.6 ± 1.9 years), weight (66.3 ± 14.8 kg), and height (173.4 ± 9.1 cm). The experimental protocol was approved by the ethics committee initiated by Shenzhen MileBot Robotics Co., Ltd in May 2023. All participants signed a written informed consent form prior to the experimental sessions.

TABLE II
STATISTICAL INFORMATION OF THE SUBJECTS

Subject	Gender	Age(y)	Weight(kg)	Height(cm)
1	Male	25	81	185
2	Male	25	70	178
3	Male	26	78	177
4	Male	24	57	172
5	Male	25	74	183
6	Male	30	87	181
7	Male	27	72	172
8	Female	23	46	159
9	Female	26	48	160
10	Female	25	50	167

During the experiments, participants performed five specific tasks at their own pace: walking, ascending stairs, descending stairs, squatting, and standing up. These tasks are outlined in Table III and depicted in Fig. 9. Note that each participant underwent a six-minute pre-training session to become familiar with each task.

Throughout data collection, the exoskeleton was powered on and operated in a transparent mode to allow the wearer to comfortably perform multiple tasks, and the motion frequency

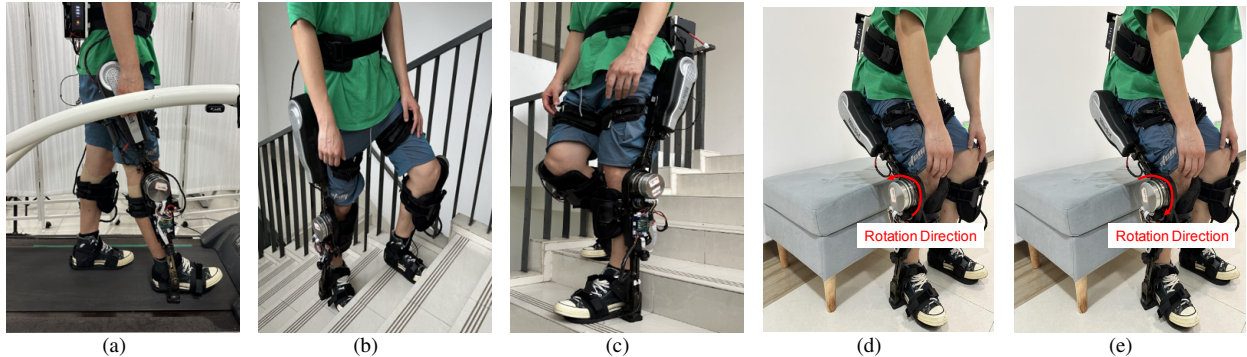


Fig. 9. Participants wearing the exoskeleton perform various tasks: (a) Walking; (b) Ascending stairs; (c) Descending stairs; (d) Squatting; (e) Standing up.

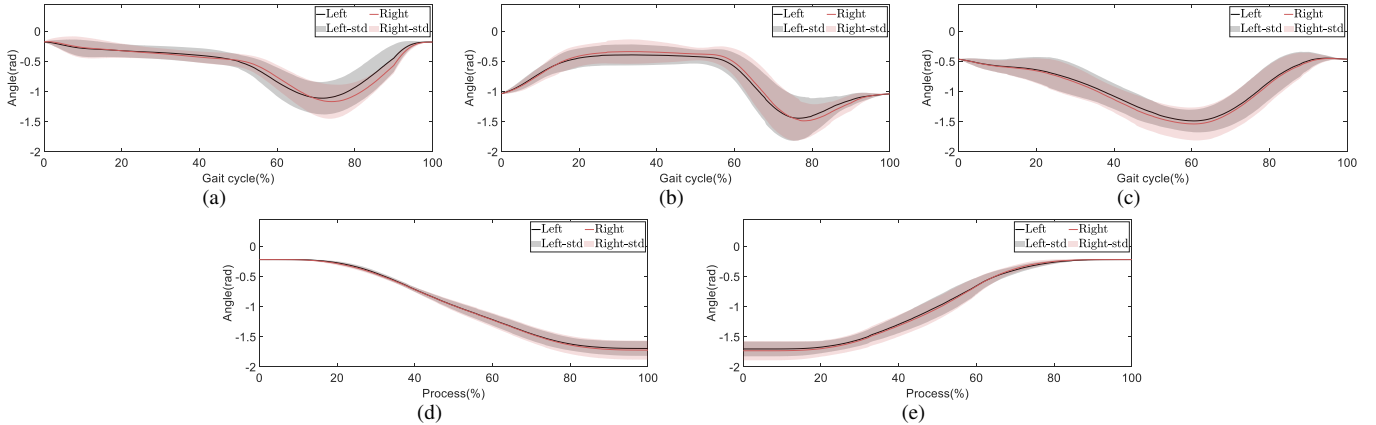


Fig. 10. Gait profiles of the knees over different tasks: (a) Walking; (b) Ascending stairs; (c) Descending stairs; (d) Squatting; (e) Standing up. The mean trajectory of the right knee is depicted by a solid red line, accompanied by a red-shaded area that indicates its standard deviation. Similarly, the mean trajectory of the left knee is illustrated by a solid black line, with the corresponding standard deviation represented by a black-shaded area. The RMSEs (rad) for the trajectories of the two legs across different tasks for all ten subjects are as follows: (a) 0.082; (b) 0.083; (c) 0.143; (d) 0.031; (e) 0.034.

was recorded using (29). During squatting and standing tasks, operating the exoskeleton solely in transparent mode was found to induce noticeable discomfort for the wearer as his or her weight was not properly supported. To mitigate this, the exoskeleton applies a constant torque to support the wearer, with the magnitude of the torque meticulously adjusted for each individual to ensure comfortable movement. In addition, Fig. 10 presents the knee joint angle profiles for all ten subjects under different tasks, and the constructed dataset was used to train the anomaly detection and task translation modules.

TABLE III
MUTIPLE TASKS PERFORMED BY THE PARTICIPANTS

Task	Description
Walking	To walk at a comfortable pace.
Ascending stairs	To ascend a flight of stairs at a comfortable pace.
Descending stairs	To descend a flight of stairs at a comfortable pace.
Squatting	To squat and hold the position for a brief period.
Standing up	To stand up from a seated position.

Remark 5: From Fig. 2, the ground reaction force can be expressed as $\mathbf{F}_g = [F_x, F_y]^T$, with F_x being the component parallel to the ground and F_y perpendicular to the ground. Then, the resulting torque on the knee joint is specified as

$$\tau_g = F_x L_s \cos(q_{\text{hip}} + q_{\text{knee}}) + F_y L_s \sin(q_{\text{hip}} + q_{\text{knee}}). \quad (62)$$

During the ground walking, the vertical component F_y predominates in the ground reaction force [22], and F_x is relatively small due to the relatively slow speed (and experimental data show $q_{\text{hip}} + q_{\text{knee}}$ in (62) ranged from -0.24 rad to

0.17 rad). Additionally, because the ankle joint is passive, the forces exerted by the wearer on it further attenuate the impact of the ground reaction forces on the knee joint. Hence, the resulting torque τ_g is relatively small in this paper. Furthermore, τ_g can be treated as disturbance [57] and mitigated with disturbance rejection techniques in position control.

Next, the gravitational torque, i.e., $\mathbf{g}(\mathbf{q})$ in (1), varies according to the hip and knee joints. However, since the hip joints of our developed exoskeleton are inactive, this paper treats the thigh as the load on the knee joint and describes the gravitational torque for both the stance and the swing phases as $\mathbf{g}(\mathbf{q}) = \frac{1}{2} m_t L_t \sin q_{\text{knee}}$, where m_t and L_t are the mass of thigh and respective distances of the center of mass of the thigh from knee joint.

VIII. RESULTS

A. Anomaly Detector

Before training the anomaly detector, the min-max normalization technique was applied to reformat the sensory data of the exoskeleton robot and ensure scale uniformity. When the participant wearing the exoskeleton could easily perform the task, the collected data were considered normal. Otherwise, they were regarded as abnormal due to physical conflicts between the human and robot.

The architecture of the anomaly detection network developed in this study is presented in Table IV. Note that the parameters for the sliding window width and the number of

channels have been established as $L_s = 100$ and $N_c = 10$, respectively.

TABLE IV
THE ARCHITECTURE OF THE DETECTION NETWORK

Layer	Input size	Output size
Flatten	(100,10)	(1000,1)
FC ^[1]	(1000,1)	(400,1)
FC $(\mu, \sigma)^{[2]}$	(400,1)	(50,1)
FC	(50, 1)	(400,1)
FC	(400, 1)	(1000,1)
Reshape	(1000,1)	(100,10)

¹ FC denotes fully-connected layer.

² μ and σ are mean and variance of the latent variables respectively.

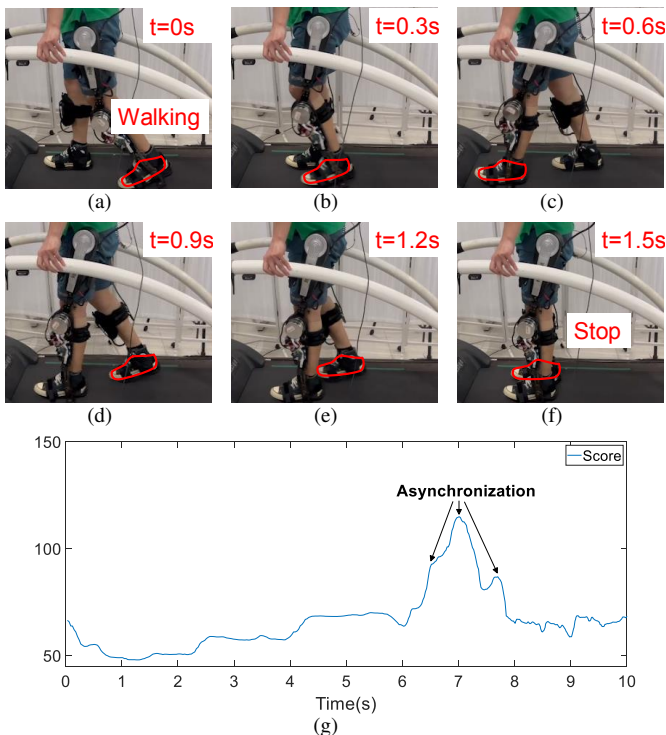


Fig. 11. (a)-(f) Snapshots of conflict due to asynchronization; (g) anomaly score during asynchronization. The red contour represents the foot during the stepping motion.

During the experiment, a participant intentionally held the robot to simulate conflict. The output of the detection network in this condition is shown in Fig. 11. The reconstruction error significantly increased when the conflict arose, indicating the wearer's discomfort. This finding highlighted that the anomaly could be successfully detected. Furthermore, the performance of the detection network was validated in another simulated conflict, where the participant lost balance due to fatigue. The results are shown in Fig. 12, further reinforcing the network's capacity to successfully detect such conflicts.

The comparison results are shown in Fig. 13. The detection performance was evaluated using the receiver operating characteristic (ROC) curve, which indicates how well a classification model can distinguish classes. In general, a larger area under the curve (AUC) indicates better performance. Fig. 13 shows that the anomaly detection network incorporating both angular and force information demonstrated a higher AUC than systems relying on single sensory input across two

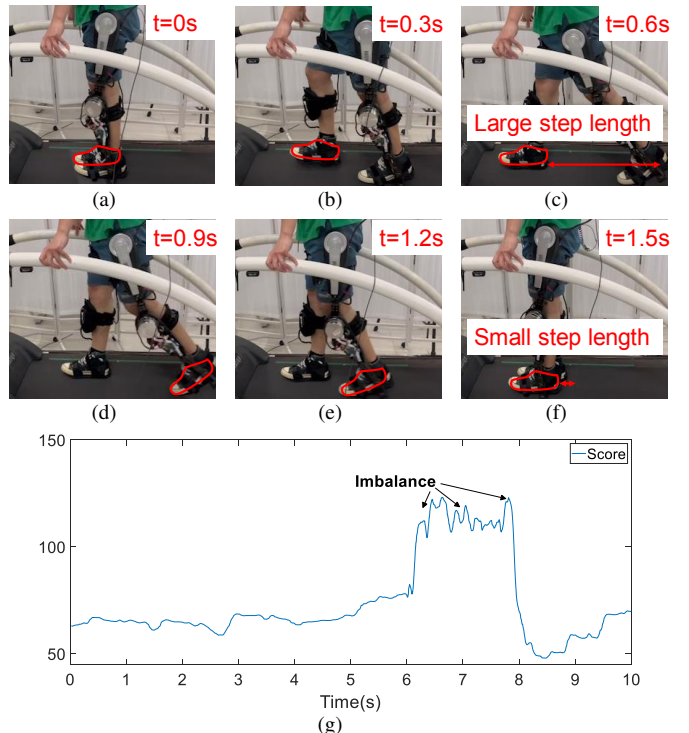


Fig. 12. (a)-(f) Snapshots of conflict due to imbalance; (g) anomaly score during imbalance. The red contour represents the foot during the stepping motion.

scenarios(i.e., asynchronization and imbalance). This finding highlights that the proposed anomaly detection network enables more precise detection, owing to its ability to handle diverse anomaly scenarios with specific manifestations. For instance, in the presence of asynchronization between the human and robot, the interaction torque rapidly increased. Conversely, in cases of imbalance due to human fatigue, angular information on the human limb, such as encoder signals, changed more significantly.

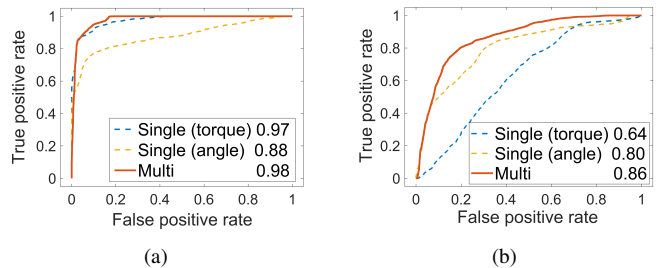


Fig. 13. AUC values (shown in the legend) and the ROC curve of multi-modal detection in comparison with single input systems (using only the torque or encoder information) in two scenarios: (a) asynchronization; (b) imbalance.

B. Task Translator

To accommodate trajectories across different tasks, the collected data were used to train a task translator. This process was modeled as a regression problem to promote generalization across diverse tasks. Owing to the limited sample size, we used a leave-one-out cross-validation approach and applied various techniques to address the regression problem, namely ridge regression, KNN, GPR, XGBoost, GBoost, SVM, and NN.

Trajectories were encoded into weight matrices corresponding to distinct tasks to allow these techniques to predict the

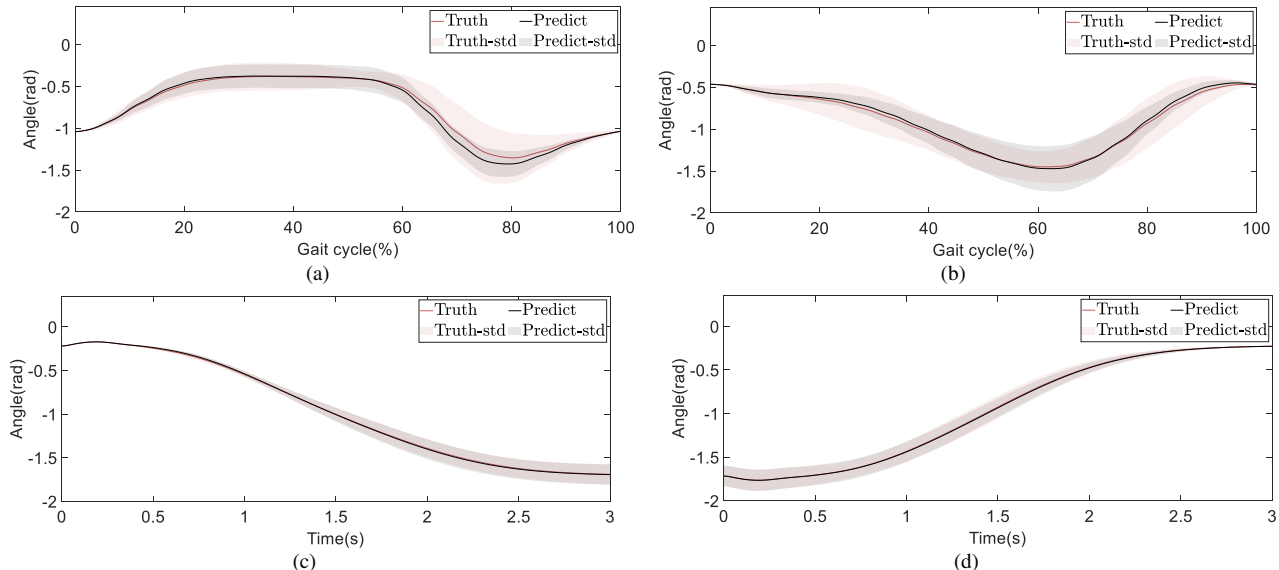


Fig. 14. Translation results across different tasks: (a) Ascending stairs; (b) Descending stairs; (c) Squatting; (d) Standing up. The red solid line represents the mean of the true profile, with the red shade indicating its standard variation. Conversely, the black solid line indicates the prediction from the task translator, with the surrounding black shade denoting its standard variation.

TABLE V
TRANSLATION RESULTS FOR ASCENDING STAIRS

J	Ridge	KNN	GPR	XGBoost	GBoost	SVM	NN
15	4.74	5.12	5.34	6.57	5.61	4.89	2.94
20	4.81	5.19	5.31	6.44	5.63	5.06	3.33
25	4.87	5.23	5.39	6.74	5.91	5.08	3.97

Note: The RMSE values are presented in degree units.

J is the kernel number for rhythmic movement.

transformation of the weight matrix from one task to another, for example, the transition from walking to ascending stairs. In the assessment of the regression outcome, both the ground truth and the predicted result are transformed into joint space from weight matrices. Subsequently, the root mean square error (RMSE) within the joint space was used as the evaluation metric for this regression task. The RMSE values are expressed in degree units. A comparison of the translation from walking to ascending stairs, using the aforementioned techniques, is presented in Table V.

The experimental results indicate that the NN-based translator exhibited superior performance among the compared models. In determining the number of kernels for optimization, a larger quantity of kernels enables the DMP to express more detailed trajectory features. However, this concurrently leads to an increase in the number of optimization variables, which consequently prolongs the time required for HIL optimization. To better balance the online computation and the representation, it is selected that $J = 20$ based on practical experience.

Upon ascertaining the kernel number for the rhythmic motion, the same approaches were used to execute the translation into discrete movements, specifically, the transitions between the squatting and standing postures. The translation outcomes for standing are summarized in Table VI. Among the evaluated methods, the NN outperformed the other techniques and was thus selected for the translation of these discrete movements. Considering both optimization efficiency and expression of DMP, the final kernel number was selected as $J_d = 15$.

TABLE VI
TRANSLATION RESULTS FOR STANDING

J_d	Ridge	KNN	GPR	XGBoost	GBoost	SVM	NN
10	4.54	4.60	4.69	4.35	4.55	4.43	2.71
15	4.81	4.87	4.86	4.66	4.86	4.69	2.89
20	4.95	5.01	4.97	4.83	4.75	4.87	2.95

Note: The RMSE values are presented in degree units.

J_d is the kernel number for discrete movement.

The number of kernels for rhythmic movement is set as $J = 20$.

Hence, within the framework of the task translator, we selected the NN for translation. The translation results for all ten subjects, derived from the application of the leave-one-out cross-validation, are visualized in Fig. 14. Note that the reproduced profile aligns satisfactorily with the collected gait profile across different tasks, despite the limitations of a small dataset. This is evident in the metric of the average RMSE, which yields values of 3.33 for ascending stairs, 2.64 for descending stairs, 2.93 for squatting, and 2.89 for standing up.

The attributes of these participants, along with their selected walking speeds, are summarized in Table VII.

TABLE VII
CHARACTERISTICS OF SUBJECTS IN HIL

Subject	Gender	Age(y)	Weight(kg)	Height(cm)	Speed(m/s)
1	Male	23	65	172	0.6
2	Male	30	85	183	0.7

The proposed variable impedance controller, described by (3),(4) and (55), was implemented in the exoskeleton robot to assist the human while detecting and relaxing physical conflicts. The impedance parameters were set as follows: $C_d = 15I_2$, $K_d = 13I_2$ where I_2 is a 2×2 identity matrix. The parameters of the weighting function were set as $\lambda_1 = 1$, $\chi_1 = 10$, $\chi_2 = 12$ and $\lambda_2 = 1$; and the control

parameters were set as $K_v = 10^{-3}I_2$ and $K_z = 25I_2$. The performance of the variable impedance controller was initially verified in walking tasks. The desired trajectories, actual joint trajectories, controller outputs, and estimated interaction torques for the left and right legs are illustrated in Fig. 15 and Fig. 16. The RMSE of the position-tracking error for the left and right legs is 0.0996 rad and 0.1149 rad, respectively.

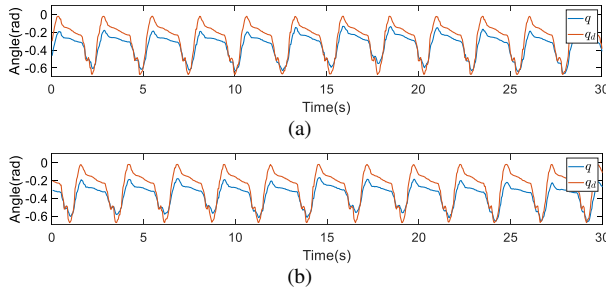


Fig. 15. Joint position and desired position in the walking task: (a) Left knee; (b) Right knee.

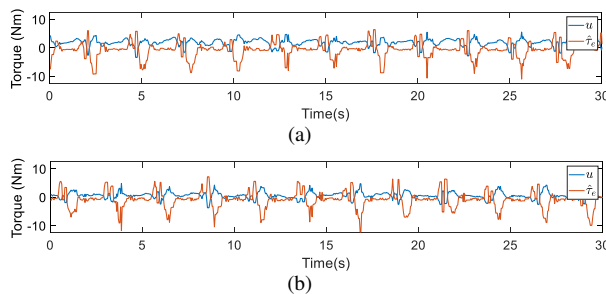


Fig. 16. Controller outputs and estimated interaction torques in the walking task: (a) Left knee; (b) Right knee.

When the joint trajectory lags behind the desired trajectory, the controller outputs a positive force to assist walking, while ensuring the realization of the target impedance model. Moreover, experimental outcomes in scenarios involving anomalies are presented in Fig. 17. The subject was instructed to resist the exoskeleton intentionally during the interval of 14 – 26 seconds, as referenced in the 23rd second of the supplementary material. During this period, the impedance parameters decreased (i.e., $w(s)$) when the anomaly score increased, relaxing the conflicts. The adjustment of impedance was continuous as the change in $w(s)$ was smooth, thereby ensuring safe human-robot interaction. The impedance vector z was around zero, proving the realization of variable impedance. Leveraging the proposed anomaly-aware variable impedance controller, we aligned the trajectory improvement through Bayesian optimization in an online manner, without undermining the safety. An additional frequency response analysis was performed to further affirm the stability of the controller within the exoskeleton system, the details of which are provided in the appendix.

To evaluate the performance of various participants in the walking task, we used the metric defined in (31) to guide trajectory optimization. Only the motors in the knees were activated to aid the wearers, such that the weight matrix W was reduced to a simple weight vector. During the initial phase of standing, the first 10 elements of the weight vectors, which represent the encoded trajectory, were similar across

all walking tasks. To alleviate the computational complexity, these elements were fixed to the mean of the data. The assistive profile was updated upon every seventh heel strike. The initial six gaits were reserved for recording sensor signals to evaluate the performance with human interaction, and the final gait was input to the Bayesian optimization algorithm. This approach prevented any sudden changes in the assistive profile that may have affected the balance of the wearers during consistent walking.

Note that the proposed method encodes the trajectories into a weighting matrix and searches the optimal configuration for those trajectory parameters. Since the optimal trajectory parameters are usually around the normal human walking trajectory, we set the parameter space to be within $\pm 30\%$ of the weighting vector of the discovered optimal trajectory, which is sufficient to cover the optimal trajectory and also able to improve the searching efficiency.

Subsequently, we halved the boundaries whenever the optimal vector remained static over the last ten steps. This method allowed the optimization process to refine the optimal weights, thereby enhancing the search efficiency without compromising the convergence certainty. The objective of the optimization process is to identify the optimal weighting vector that minimizes the cost, and this operation is executed in real-time. Specifically, it took around 14 minutes for the proposed HIL method to achieve the optimal configuration for each λ , i.e., 60 iterations, given seven steps per cycle. In addition, a total of 10 restarts were executed to bypass local optima.

C. HIL Optimization

Fig. 18 illustrates the HIL optimization outcomes. The blue and black solid lines correspond to the optimal trajectories when $\lambda = 1$ and 0, respectively; the red trajectory depicts the mean and variance of the optimization outcomes for λ values between (0, 1), i.e., $\lambda = 0.25, 0.5, 0.75$. The results revealed that an optimal trajectory with $\lambda = 1$ tended towards lazy assistance because the optimization term overly emphasized trajectory alignment, thereby causing the trajectory to converge to a curve with a smaller stretch amplitude. In contrast, for $\lambda = 0$, where the cost function consisted solely of the anomaly scores output by the NN, the final optimized trajectory exhibited heightened and frequent fluctuations. When λ ranged between 0 and 1, its effect on the trajectory optimization was significantly similar. This may be attributable to λ eliminating the gap between the dataset and participant actions during optimizing based on the anomaly score. Essentially, the first term in (31) was optimized to a lower value, and then the trajectory details were improved according to the human machine interaction results, thereby minimizing conflict and enhancing comfort.

Additional tests were performed to evaluate the effectiveness of the optimization results. Specifically, an indirect, quantitative evaluation of user comfort and assistance effectiveness was performed using EMG signals from the TA and QF, along with the average power transferred by the exoskeleton per step. The metrics were averaged for both the left and right legs over a single step. Furthermore,

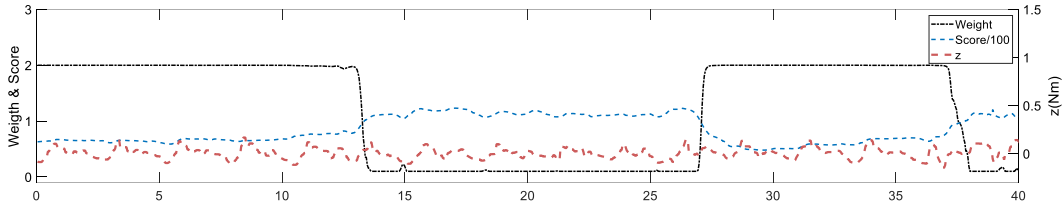


Fig. 17. Experimental results using the proposed variable impedance controller: The impedance parameters were scaled down (black dashed line) when the anomaly score increased (blue solid line), thereby alleviating the conflicts. The adjustment of impedance is continuous as the change in $w(s)$ is smooth, ensuring safe human-robot interaction. The impedance vector (red dashed line) was around zero, proving the realization of the variable impedance model.

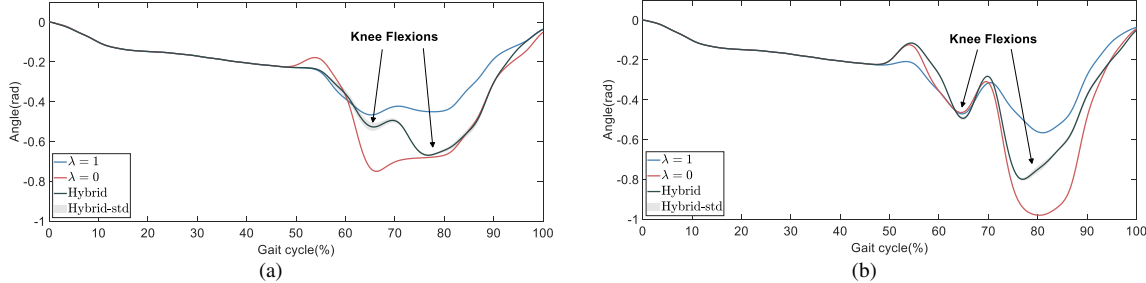


Fig. 18. HIL optimization results of different hyperparameters λ for different participants: (a) Participant 1; (b) Participant 2. The blue and red solid lines represent the optimized trajectories in the context of $\lambda = 1$ and $\lambda = 0$, respectively. The black solid line is the mean of the trajectories, with $\lambda \in (0, 1)$, and the surrounding black shade indicates its standard variation.

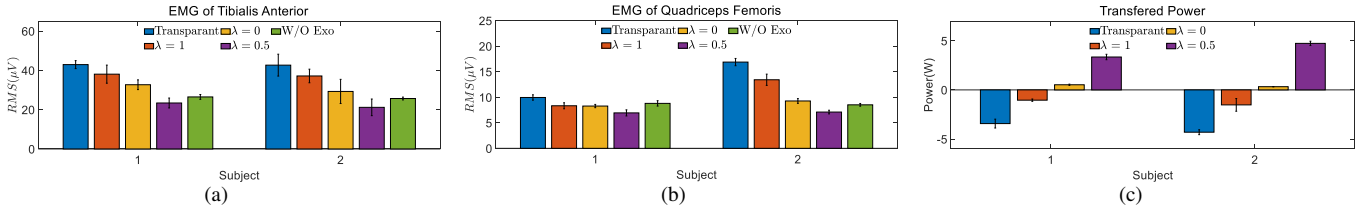


Fig. 19. Comparative evaluation of different modes across participants: (a) RMS of EMG signals from the tibialis anterior, indicative of user comfort; (b) RMS of EMG signals from the quadriceps femoris; (c) Average power transferred by the exoskeleton per step, with negative and positive values indicating resistance and assistance, respectively.

the transferred power was calculated based on the estimated interaction torque multiplied by the motor velocity. Fig. 19 shows the experimental outcomes in the transparent mode, with the optimized trajectory and without exoskeleton wear. Considering the minimal influence of λ on the trajectory optimization results, we included only cases where λ equaled 0, 0.5, and 1. The outcomes suggested that a trajectory produced with $\lambda = 0.5$ could not only ensure optimal comfort, as evidenced by the small amplitude of the EMG signal, but also provide effective assistance, i.e., maximum power transfer under all conditions.

Remark 6: The HIL results have been improved with respect to the existing works because: (i) It has reduced the time cost (e.g., 64 minutes with four iterations in [10]). (ii) There is always a trade-off between faster optimization and more variables. Although other methods may be faster, the proposed method incorporates the highest number of optimization variables to date (i.e., 20 vs. 4 in the literature [21]), thereby capturing more in-depth details of different wearers' walking habits, resulting in a larger exploration space and enabling better generalization across diverse tasks. (iii) Unlike other studies that rely on time-consuming metabolic rate measurements [10], the proposed method focuses on the improvement

of comfort using anomaly scores, thereby saving time by eliminating the need for these measurements.

D. Translated Assistance

The trajectories derived from HIL optimization were used to accommodate various tasks, including ascending stairs, descending stairs, and the combined tasks of squatting and standing up. Fig. 20 offers a visualization of these translated trajectories along with the trajectory acquired in the transparent mode. Within our dataset, the average trajectory is referred to as the "normative trajectory".

The findings demonstrated that, compared with the normative trajectories, the translated trajectories could enable the provision of appropriate assistance, as referenced in the 2 minutes and 48 seconds of the supplementary material. When ascending stairs, the elevated stepping leg received assistance in knee flexion to facilitate foot landing. Conversely, for descending stairs, the translated trajectories were consistent with the desired trajectory, which allows the robot to support the body weight through the impedance controller. Similarly, tasks such as squatting and standing up were assisted by weight support achieved through trajectory optimization. At the beginning of the squatting task, the translated trajectories exhibited an upward curve that deviated from the immediate

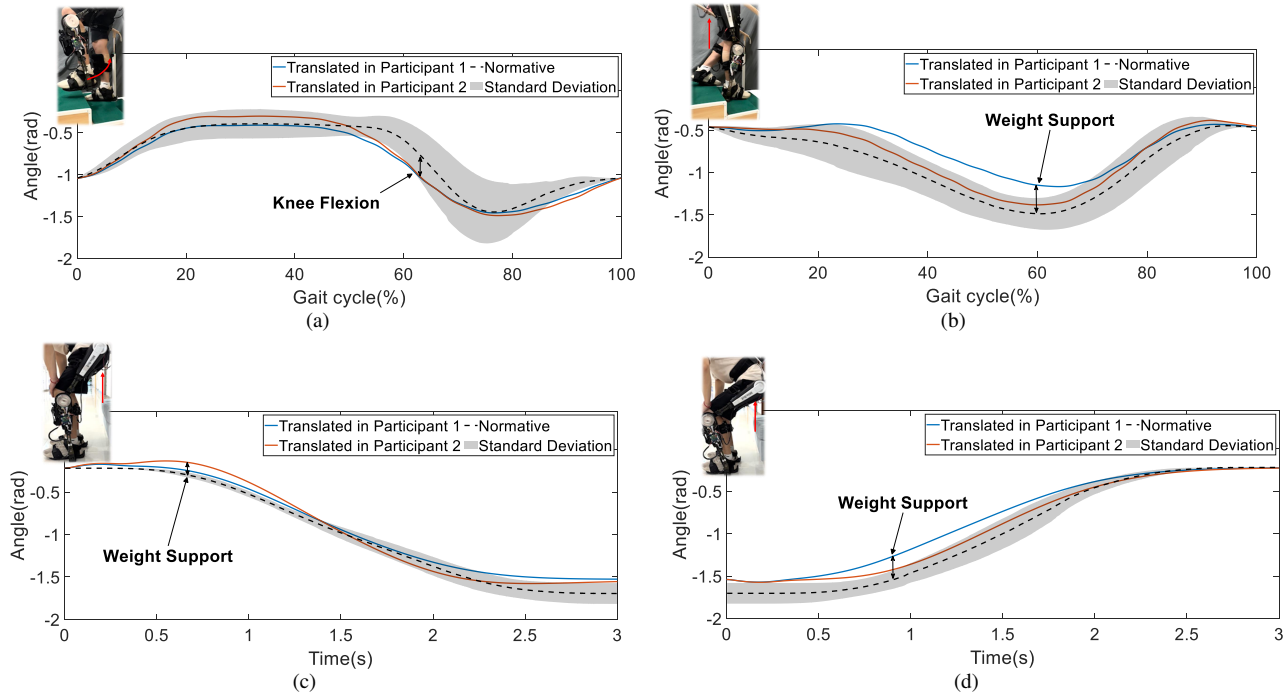


Fig. 20. Translation of optimized assistance across different tasks: (a) Ascending stairs; (b) Descending stairs; (c) Squatting; (d) Standing up. The red arrows denote the corresponding interactive forces exerted by the exoskeleton assistance. The blue and red solid lines represent the translation of optimized trajectories from Participants 1 and 2, respectively. The black dashed line represents the prediction from the task translator, with the surrounding black shade denoting its standard variation.

decline observed in the normative trajectory, suggestive of preparatory actions for weight support.

To validate the effectiveness of the translated assistance, we compared the EMG signals of the TA and QF and the average power transfer per step under different conditions: transparent mode, normative mode, optimized mode, and a scenario without the exoskeleton, as summarized in Table VIII.

TABLE VIII
MODES

Mode	Character
Transparent	Unrestricted mobility without apparent resistance.
Normative	q_d is the mean trajectory from the database.
Translated	q_d is the translation result of the optimized trajectory.
W/O Exo	Unrestricted mobility without assistance.

The findings from these experiments are illustrated in Fig. 21. Notably, the tasks of squatting and standing up were treated as one combined task, with a one-second separation used to distinguish the two. In terms of minimizing the amplitude of the EMG signal and augmenting power transfer, the translated assistance demonstrated a modest improvement over the normative mode. This outcome suggested that the optimized and translated trajectories converged in the same latent space. Specifically, the translator, which was trained using the collected dataset, could be directly applied to the results of the HIL optimization. Our proposed task translator could thus enhance comfort and assistance across various tasks based on the HIL results from the walking task. Therefore, we not only optimized the task trajectories that posed challenges for online optimization but also reduced the time required for task transfer.

IX. DISCUSSION AND CONCLUSIONS

A. Limitations

The limitations of our method include the following

- 1) The proposed HIL method involves optimizing multiple dimensions for encoded trajectories. Although this approach can capture the walking habits of different individuals and be generalized to multiple tasks, the trade-off is an increase in the overall time cost as more joints are simultaneously optimized.
- 2) Due to the limitation of the current mechanical design, the developed exoskeleton would require additional connectors to activate the hip joints for specific wearers (e.g., female subjects with slim bodies). However, the addition of these connectors would significantly affect the comfort of wearers. Hence, optimization at the hip joint was not considered in this study.
- 3) The transition between different desired trajectories (e.g., from walking to ascending) is not automatically triggered. For a specific task requiring robot assistance, trajectory parameters must be manually switched to the corresponding settings. Subsequently, these parameters are continuously updated using the proposed HIL method to better suit the specific wearer. The function of automatic transition may be achieved with a support vector machine (SVM) or extended Kalman filter [16].

Those limitations will be addressed in future work.

B. Conclusions

This paper proposes a novel adaptation framework for exoskeleton robots to customize the assistance provided to

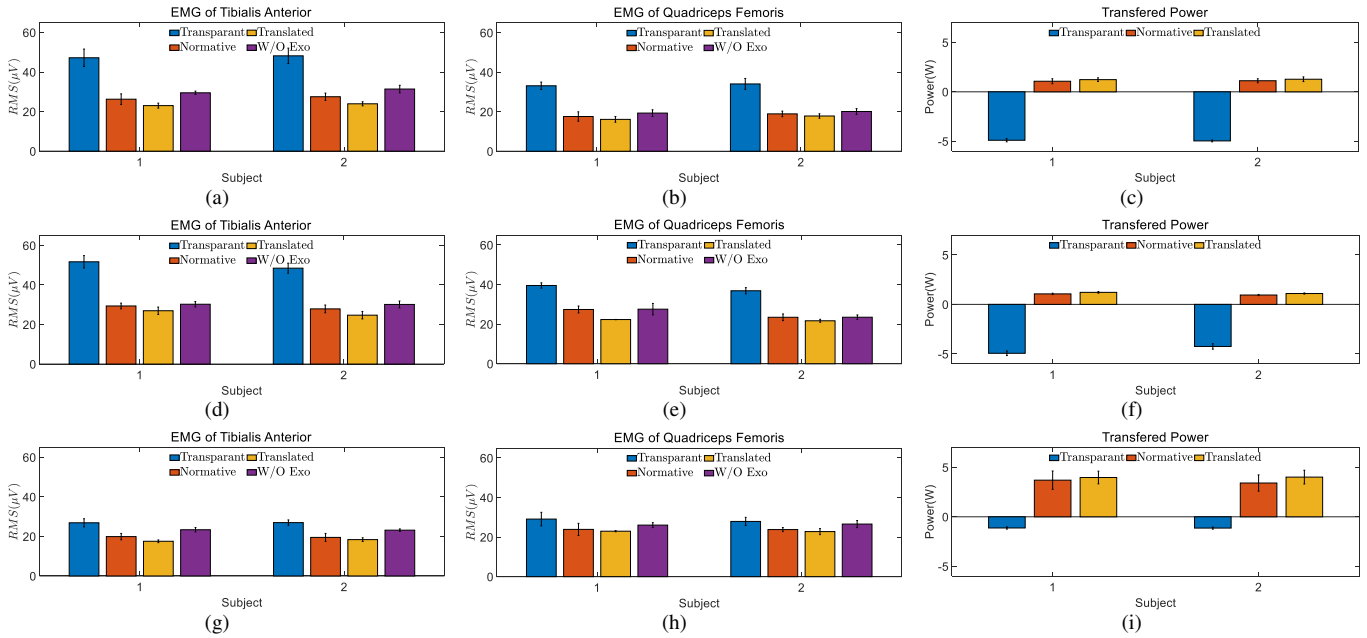


Fig. 21. Comparative evaluation of different modes across participants. Translation results for (a)-(c) stair ascent; (d)-(f) stair descent; (g)-(i) squatting and standing up; Each column depicts different metrics: RMS of EMG signals from Tibialis Anterior and RMS of EMG signals from Quadriceps Femoris, indicating user comfort; and average power transferred by the exoskeleton per step, with negative values indicating resistance and positive values denoting assistance.

different wearers during multiple tasks. Specifically, the individualized trajectory is generated using DMP and online optimization, which can then be transformed to other trajectories for different tasks with the trained NN. The individualized trajectory is incorporated in the variable impedance controller to drive the robot to provide assistance while ensuring a safe interaction. The advantages of the proposed framework can be summarized as follows: 1) an anomaly detection network is applied to improve wearing comfort during HIL optimization and relax potential conflicts during implementation; 2) the proposed approach is data-efficient with HIL adaptation ability, allowing the robot to promptly adapt to new users in new tasks, even with limited samples; and 3) the framework requires only proprioceptive sensors and is thus easy to implement. The proposed method is evaluated using the training samples of 10 users and validation samples of two new users. Experiments and comparative studies are performed over four tasks (i.e., walking, stair ascent, stair descent, and sit-to-stand) to demonstrate the effectiveness of the exoskeleton robot. The intellectual merit and broader impacts for the proposed method can be summarized as follows.

First, this paper introduces an innovative framework that uses interactive learning techniques to facilitate efficient and individualized adaptations for lower-limb exoskeletons. The proposed framework effectively utilizes the human-in-the-loop feature, i.e., exploration of the interaction between the exoskeleton and wearer to achieve generalized assistance across various tasks for diverse wearers. This aspect is particularly crucial, given the intricate and dynamic nature of human movements.

Second, the provision of generalized and optimized assistance, coupled with the reliance on only proprioceptive sensors, can help catalyze the widespread deployment of lower-

limb exoskeletons in both industrial settings and homecare applications. This ability is expected to have a transformative impact on individuals, not only enhancing the quality of life but also driving changes in lifestyle. This innovation can help address the growing labor shortage in various sectors, which is crucial for managing the challenges posed by a rapidly aging society.

REFERENCES

- [1] M. P. De Looze, T. Bosch, F. Krause, K. S. Stadler, and L. W. O'sullivan, "Exoskeletons for industrial application and their potential effects on physical work load," *Ergonomics*, vol. 59, no. 5, pp. 671–681, 2016.
- [2] A. B. Zoss, H. Kazerooni, and A. Chu, "Biomechanical design of the berkeley lower extremity exoskeleton (BLEEX)," *IEEE/ASME Transactions on mechatronics*, vol. 11, no. 2, pp. 128–138, 2006.
- [3] X. Li, X. Zhang, X. Li, J. Long, J. Li, L. Xu, G. Chen, and J. Ye, "Bear-h: An intelligent bilateral exoskeletal assistive robot for smart rehabilitation," *IEEE Robotics & Automation Magazine*, vol. 29, no. 3, pp. 34–46, 2021.
- [4] A. Esquenazi, M. Talaty, and A. Jayaraman, "Powered exoskeletons for walking assistance in persons with central nervous system injuries: a narrative review," *PM&R*, vol. 9, no. 1, pp. 46–62, 2017.
- [5] L. Brenner, "Exploring the psychosocial impact of ekso bionics technology," *Archives of Physical Medicine and Rehabilitation*, vol. 97, no. 10, p. e113, 2016.
- [6] M. Iizuka and Y. Ikeda, "Regulation and innovation under the 4th industrial revolution: The case of a healthcare robot, hal by cyberdyne," *Technovation*, vol. 108, p. 102335, 2021.
- [7] T. Teramae, T. Noda, and J. Morimoto, "Emg-based model predictive control for physical human–robot interaction: Application for assist-as-needed control," *IEEE Robotics and Automation Letters*, vol. 3, no. 1, pp. 210–217, 2017.
- [8] X. Zhang, Y. Shu, Y. Chen, G. Chen, J. Ye, X. Li, and X. Li, "Multi-modal learning and relaxation of physical conflict for an exoskeleton robot with proprioceptive perception," in *Proceedings of the 2023 IEEE International Conference on Robotics and Automation (ICRA)*, 2023.
- [9] P. Slade, M. J. Kochenderfer, S. L. Delp, and S. H. Collins, "Personalizing exoskeleton assistance while walking in the real world," *Nature*, vol. 610, no. 7931, pp. 277–282, 2022.

- [10] J. Zhang, P. Fiers, K. A. Witte, R. W. Jackson, K. L. Poggensee, C. G. Atkeson, and S. H. Collins, "Human-in-the-loop optimization of exoskeleton assistance during walking," *Science*, vol. 356, no. 6344, pp. 1280–1284, 2017.
- [11] K.-W. Park, J. Choi, and K. K. Kong, "Iterative learning of human behavior for adaptive gait pattern adjustment of a powered exoskeleton," *IEEE Transactions on Robotics*, 2022.
- [12] P. W. Franks, G. M. Bryan, R. Reyes, M. P. O'Donovan, K. N. Gregorczyk, and S. H. Collins, "The effects of incline level on optimized lower-limb exoskeleton assistance: A case series," *IEEE Transactions on Neural Systems and Rehabilitation Engineering*, vol. 30, pp. 2494–2505, 2022.
- [13] Y. Wen, A. Brandt, J. Si, and H. H. Huang, "Automatically customizing a powered knee prosthesis with human in the loop using adaptive dynamic programming," in *2017 International Symposium on Wearable Robotics and Rehabilitation (WeRob)*. IEEE, 2017, pp. 1–2.
- [14] Y. Ding, M. Kim, S. Kuindersma, and C. J. Walsh, "Human-in-the-loop optimization of hip assistance with a soft exosuit during walking," *Science Robotics*, vol. 3, no. 15, p. eaar5438, 2018.
- [15] Y. Zhang, S. Li, K. J. Nolan, and D. Zanotto, "Adaptive assist-as-needed control based on actor-critic reinforcement learning," in *2019 IEEE/RSJ International Conference on Intelligent Robots and Systems (IROS)*. IEEE, 2019, pp. 4066–4071.
- [16] Z. Li, X. Li, Q. Li, H. Su, Z. Kan, and W. He, "Human-in-the-loop control of soft exosuits using impedance learning on different terrains," *IEEE Transactions on Robotics*, 2022.
- [17] U. H. Lee, V. S. Shetty, P. W. Franks, J. Tan, G. Evangelopoulos, S. Ha, and E. J. Rouse, "User preference optimization for control of ankle exoskeletons using sample efficient active learning," *Science Robotics*, vol. 8, no. 83, p. eadg3705, 2023.
- [18] P. Kantharaju, H. Jeong, S. Ramadurai, M. Jacobson, H. Jeong, and M. Kim, "Reducing squat physical effort using personalized assistance from an ankle exoskeleton," *IEEE Transactions on Neural Systems and Rehabilitation Engineering*, vol. 30, pp. 1786–1795, 2022.
- [19] T.-C. Wen, M. Jacobson, X. Zhou, H.-J. Chung, and M. Kim, "The personalization of stiffness for an ankle-foot prosthesis emulator using human-in-the-loop optimization," in *2020 IEEE/RSJ International Conference on Intelligent Robots and Systems (IROS)*. IEEE, 2020, pp. 3431–3436.
- [20] M. Jacobson, P. Kantharaju, H. Jeong, J.-K. Ryu, J.-J. Park, H.-J. Chung, and M. Kim, "Foot contact forces can be used to personalize a wearable robot during human walking," *Scientific Reports*, vol. 12, no. 1, p. 10947, 2022.
- [21] D. F. Gordon, C. McGreavy, A. Christou, and S. Vijayakumar, "Human-in-the-loop optimization of exoskeleton assistance via online simulation of metabolic cost," *IEEE Transactions on Robotics*, vol. 38, no. 3, pp. 1410–1429, 2022.
- [22] X. Tan, B. Zhang, G. Liu, X. Zhao, and Y. Zhao, "A time-independent control system for natural human gait assistance with a soft exoskeleton," *IEEE Transactions on Robotics*, 2022.
- [23] S. Hood, L. Gabert, and T. Lenzi, "Powered knee and ankle prosthesis with adaptive control enables climbing stairs with different stair heights, cadences, and gait patterns," *IEEE Transactions on Robotics*, 2022.
- [24] Y. Qian, H. Yu, and C. Fu, "Adaptive oscillator-based assistive torque control for gait asymmetry correction with a nsea-driven hip exoskeleton," *IEEE Transactions on Neural Systems and Rehabilitation Engineering*, vol. 30, pp. 2906–2915, 2022.
- [25] E. Reznick, K. Embry, and R. D. Gregg, "Predicting individualized joint kinematics over a continuous range of slopes and speeds," in *2020 8th IEEE RAS/EMBS International Conference for Biomedical Robotics and Biomechatronics (BioRob)*. IEEE, 2020, pp. 666–672.
- [26] S. Cheng, E. Bolívar-Nieto, C. G. Welker, and R. D. Gregg, "Modeling the transitional kinematics between variable-incline walking and stair climbing," *IEEE Transactions on Medical Robotics and Bionics*, vol. 4, no. 3, pp. 840–851, 2022.
- [27] P. Kantharaju, S. S. Vakacherla, M. Jacobson, H. Jeong, M. N. Mevada, X. Zhou, M. J. Major, and M. Kim, "Framework for personalizing wearable devices using real-time physiological measures," *IEEE Access*, 2023.
- [28] J. Kim, P. Kantharaju, H. Yi, M. Jacobson, H. Jeong, H. Kim, J. Lee, J. Matthews, N. Zavanelli, H. Kim, et al., "Soft wearable flexible bioelectronics integrated with an ankle-foot exoskeleton for estimation of metabolic costs and physical effort," *npj Flexible Electronics*, vol. 7, no. 1, p. 3, 2023.
- [29] C.-C. Cheah and D. Wang, "Learning impedance control for robotic manipulators," *IEEE Transactions on Robotics and Automation*, vol. 14, no. 3, pp. 452–465, 1998.
- [30] M. Sharifi, A. Zakerimanesh, J. K. Mehr, A. Torabi, V. K. Mushahwar, and M. Tavakoli, "Impedance variation and learning strategies in human-robot interaction," *IEEE Transactions on Cybernetics*, 2021.
- [31] Y. Huo, X. Li, X. Zhang, and D. Sun, "Intention-driven variable impedance control for physical human-robot interaction," in *2021 IEEE/ASME International Conference on Advanced Intelligent Mechatronics (AIM)*. IEEE, 2021, pp. 1220–1225.
- [32] L. Rozo, S. Calinon, D. G. Caldwell, P. Jimenez, and C. Torras, "Learning physical collaborative robot behaviors from human demonstrations," *IEEE Transactions on Robotics*, vol. 32, no. 3, pp. 513–527, 2016.
- [33] F. Ficuciello, L. Villani, and B. Siciliano, "Variable impedance control of redundant manipulators for intuitive human–robot physical interaction," *IEEE Transactions on Robotics*, vol. 31, no. 4, pp. 850–863, 2015.
- [34] Y.-C. Pai, B. Maki, K. Iqbal, W. McIlroy, and S. Perry, "Thresholds for step initiation induced by support-surface translation: a dynamic center-of-mass model provides much better prediction than a static model," *Journal of Biomechanics*, vol. 33, no. 3, pp. 387–392, 2000.
- [35] X. Zhang, L. Sun, Z. Kuang, and M. Tomizuka, "Learning variable impedance control via inverse reinforcement learning for force-related tasks," *IEEE Robotics and Automation Letters*, vol. 6, no. 2, pp. 2225–2232, 2021.
- [36] M. Bogdanovic, M. Khadiv, and L. Righetti, "Learning variable impedance control for contact sensitive tasks," *IEEE Robotics and Automation Letters*, vol. 5, no. 4, pp. 6129–6136, 2020.
- [37] C. Yang, C. Zeng, C. Fang, W. He, and Z. Li, "A dmbs-based framework for robot learning and generalization of humanlike variable impedance skills," *IEEE/ASME Transactions on Mechatronics*, vol. 23, no. 3, pp. 1193–1203, 2018.
- [38] Z. Jin, A. Liu, W.-a. Zhang, and L. Yu, "An optimal variable impedance control with consideration of the stability," *IEEE Robotics and Automation Letters*, vol. 7, no. 2, pp. 1737–1744, 2022.
- [39] A. Albu-Schäffer, C. Ott, and G. Hirzinger, "A unified passivity-based control framework for position, torque and impedance control of flexible joint robots," *The International Journal of Robotics Research*, vol. 26, no. 1, pp. 23–39, 2007.
- [40] C. C. Cheah and X. Li, *Task-space sensory feedback control of robot manipulators*. Springer, 2015, vol. 73.
- [41] S. Arimoto, "Control theory of nonlinear mechanical systems," *A Passivity-based and Circuit-theoretic Approach*, 1996.
- [42] M. M. Olsen and H. G. Petersen, "A new method for estimating parameters of a dynamic robot model," *IEEE transactions on robotics and automation*, vol. 17, no. 1, pp. 95–100, 2001.
- [43] M. W. Spong, "Modeling and control of elastic joint robots," 1987.
- [44] C. A. Oatis, "The use of a mechanical model to describe the stiffness and damping characteristics of the knee joint in healthy adults," *Physical Therapy*, vol. 73, no. 11, pp. 740–749, 1993.
- [45] S. Han, H. Wang, and H. Yu, "Human–robot interaction evaluation-based aac control for upper limb rehabilitation robots driven by series elastic actuators," *IEEE Transactions on Robotics*, 2023.
- [46] X. Li, Y. Liu, and H. Yu, "Iterative learning impedance control for rehabilitation robots driven by series elastic actuators," *Autom.*, vol. 90, pp. 1–7, 2018.
- [47] Y. Zimmermann, E. B. Küçüktabak, F. Farshidian, R. Riener, and M. Hutter, "Towards dynamic transparency: Robust interaction force tracking using multi-sensory control on an arm exoskeleton," in *2020 IEEE/RSJ International Conference on Intelligent Robots and Systems (IROS)*. IEEE, 2020, pp. 7417–7424.
- [48] S. Lin, R. Clark, R. Birke, S. Schönborn, N. Trigoni, and S. J. Roberts, "Anomaly detection for time series using vae-lstm hybrid model," *ICASSP 2020 - 2020 IEEE International Conference on Acoustics, Speech and Signal Processing (ICASSP)*, pp. 4322–4326, 2020.
- [49] Y. Qian, Y. Wang, C. Chen, J. Xiong, Y. Leng, H. Yu, and C. Fu, "Predictive locomotion mode recognition and accurate gait phase estimation for hip exoskeleton on various terrains," *IEEE Robotics and Automation Letters*, vol. 7, no. 3, pp. 6439–6446, 2022.
- [50] D. Park, Y. Hoshi, and C. C. Kemp, "A multimodal anomaly detector for robot-assisted feeding using an lstm-based variational autoencoder," *IEEE Robotics and Automation Letters*, vol. 3, pp. 1544–1551, 2017.
- [51] A. J. Ijspeert, J. Nakanishi, H. Hoffmann, P. Pastor, and S. Schaal, "Dynamical movement primitives: learning attractor models for motor behaviors," *Neural Computation*, vol. 25, no. 2, pp. 328–373, 2013.
- [52] S. Schaal and C. G. Atkeson, "Constructive incremental learning from only local information," *Neural computation*, vol. 10, no. 8, pp. 2047–2084, 1998.
- [53] M. Kim, C. Liu, J. Kim, S. Lee, A. Meguid, C. J. Walsh, and S. Kuindersma, "Bayesian optimization of soft exosuits using a metabolic estimator

- stopping process," in *2019 International Conference on Robotics and Automation (ICRA)*. IEEE, 2019, pp. 9173–9179.
- [54] A. Mohammadi, H. J. Marquez, and M. Tavakoli, "Nonlinear disturbance observers: Design and applications to euler? lagrange systems," *IEEE Control Systems Magazine*, vol. 37, no. 4, pp. 50–72, 2017.
- [55] A. Mohammadi, M. Tavakoli, H. J. Marquez, and F. Hashemzadeh, "Nonlinear disturbance observer design for robotic manipulators," *Control Engineering Practice*, vol. 21, no. 3, pp. 253–267, 2013.
- [56] A. N. Tikhonov, "Systems of differential equations containing small parameters in the derivatives," *Matematicheskii sbornik*, vol. 73, no. 3, pp. 575–586, 1952.
- [57] Z. Li, K. Zhao, L. Zhang, X. Wu, T. Zhang, Q. Li, X. Li, and C.-Y. Su, "Human-in-the-loop control of a wearable lower limb exoskeleton for stable dynamic walking," *IEEE/ASME transactions on Mechatronics*, vol. 26, no. 5, pp. 2700–2711, 2020.

APPENDIX

Algorithm 1 Anomaly Detection

Require: $q, \dot{q}, \theta, \dot{\theta}, K(\theta - q)$

- 1: Initialize sliding window queue
- 2: **for** each new data point **do**
- 3: $\mathbf{x}_{now}^t \leftarrow (q, \dot{q}, \theta, \dot{\theta}, K(\theta - q))$
- 4: Enqueue \mathbf{x}_{now}^t to sliding window queue
- 5: **if** sliding window queue is full **then**
- 6: $\mathbf{x}_w^t \leftarrow \text{GetWindowData}()$
- 7: $\mathbf{x}^t \leftarrow \text{Flatten}(\mathbf{x}_w^t)$
- 8: $\mathbf{x}_e^t \leftarrow \text{Encoder}(\mathbf{x}^t)$
- 9: $\mu \leftarrow \text{FC}_\mu(\mathbf{x}_e^t)$
- 10: $\sigma \leftarrow \text{FC}_\sigma(\mathbf{x}_e^t)$
- 11: $\epsilon \leftarrow \text{SampleNoise}()$
- 12: $\rho \leftarrow \mu + \sigma \odot \epsilon$
- 13: $\hat{\mathbf{x}}^t \leftarrow \text{Decoder}(\rho)$
- 14: $s \leftarrow \text{CalculateMSE}(\mathbf{x}^t, \hat{\mathbf{x}}^t)$
- 15: Output: s
- 16: Dequeue from sliding window queue
- 17: **end if**
- 18: **end for**

Algorithm 2 Individualized Trajectory Generation

Require: s, \mathbf{W}, q

- 1: Initialize λ, N_a
- 2: **for** each gait **do**
- 3: $T \leftarrow \text{Duration}$
- 4: $\mathcal{J}_{new}(s, q, \mathbf{W}) \leftarrow \text{Equation(31)}$
- 5: $\mathbf{W}_{new} \leftarrow \text{Bayesian_Optimization}(\mathcal{J}_{new})$
- 6: **if** optimization finished **then**
- 7: $\mathbf{W}^* \leftarrow \mathbf{W}_{new}$
- 8: **if** translation to task A **then**
- 9: $\hat{\mathbf{W}}_A \leftarrow \mathbf{F}_r(\mathbf{W}^*)$
- 10: $q_d \leftarrow \text{DMP}(\hat{\mathbf{W}}_A)$
- 11: **else**
- 12: $q_d \leftarrow \text{DMP}(\mathbf{W}^*)$
- 13: **end if**
- 14: Output: q_d
- 15: **end if**
- 16: **end for**

Simulation of HIL Optimization

This simulation study is to validate the feasibility of the proposed method for the hip and knee joints simultaneously.

Specifically, we used the hip and knee joint trajectories of a participant as the target trajectories for optimization, referred to as q_{Sim} , which correspond to the joint trajectories that achieved the lowest cost function in real experiments. We used the mean trajectory of the knee joint from the collected data and hip joint trajectory of another participant as the initial values, which were encoded into a weighting matrix $\mathbf{W}_{initial}$ for optimization. In this simulation, the uncertainties in human interaction and network inference were implicitly considered by modeling them as noise in the weight matrix as

$$\mathbf{W}_{next} = \mathbf{W}^{\text{new}} + \mathbf{E}_\epsilon, \quad (63)$$

where \mathbf{W}^{new} represents the solution in the current iteration, and $\mathbf{E}_\epsilon \in \mathbb{R}^{N_a \times J}$ is the noise matrix symbolizing the integrated uncertainty, with parameters set as $N_a = 2$ and $J = 20$. Note that the gait frequency was normalized to $\Omega_c = 2\pi$, and the cost function was defined as

$$\mathcal{J}_{Sim}(\mathbf{W}) = MSE(q_{Sim}(t) - f_p(t, \mathbf{W}, \Omega_c)). \quad (64)$$

Then, the weighting matrix undergoes joint optimization via Bayesian optimization for both joints, and the results are shown in Fig. 22. The target trajectory is indicated by the black dashed line, while the initial trajectory and trajectory generated by the optimal weighting matrix are represented by the red and blue solid lines, respectively. The optimization process involved 147 iteration steps. The results demonstrated that the proposed method can identify the optimal weighting matrix within a reasonable time frame for both joints.

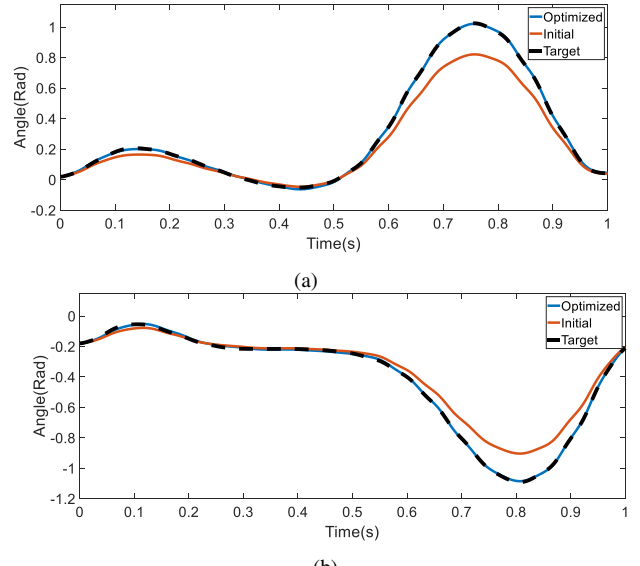


Fig. 22. Simulation results for the HIL optimization: (a) the hip joint, (b) the knee joint.

Frequency Response

To enhance the validation of the stability offered by the proposed variable impedance controller, frequency response tests were performed on the integrated actuator and exoskeleton system. During these tests, the system operated under impedance control mode without the application of external forces, degenerating the controller into a position-based control scheme. The desired joint position is used as the system input command, and the corresponding positional

responses were measured across varying frequency setups, with the proposed impedance controller operating in an open-loop configuration. The results of the numerical analysis, as illustrated in Fig. 23, depict the dynamic characteristics of the complete exoskeleton system.

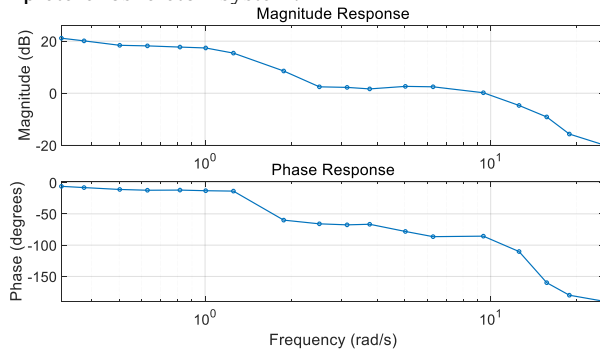


Fig. 23. Bode plot of the compliantly actuated exoskeleton system with controller operated in an open-loop. The system input is the desired joint angle (degree), and the output is the joint angle (degree).

The benchtop data acquired from this experiment reveal that the phase margin for the actuator-exoskeleton system is approximately 93° , with a gain margin nearing 15.7 dB, which demonstrate the stability and robustness of the proposed controller.



Yu Chen (Student Member, IEEE) received the B.Eng. degree in automation from Harbin Institute of Technology, Harbin, China, in 2022. He is currently working toward the Ph.D. degree in control science and engineering with the Department of Automation, Tsinghua University, Beijing, China. His research interests include wearable robots and physical human-robot interaction.



Shu Miao received the M.S. degree in electrical engineering from Northeastern University, Shenyang, China, in 2019, and the Ph.D. degree in mechanical engineering from the Harbin Institute of Technology, Shenzhen, China. He is currently a Postdoctoral Fellow with the Department of Automation, Tsinghua University, Beijing, China. His research interests include robotic cell manipulation and medical robotics.



Gong Chen received the B.E. degree in mechanical engineering and automation from Shanghai JiaoTong University, Shanghai, China, in 2011, and the Ph.D. degree in biomedical engineering from the National University of Singapore, Singapore, in 2016. He is currently the CEO of Shenzhen MileBot Robotics Company Ltd., Shenzhen, China. His research interests include wearable exoskeleton and compliant actuator.



Jing Ye received Ph.D. degree in Biomedical Engineering from Waseda University in 2015. He is currently the CTO of Shenzhen MileBot Robotics Co., Ltd, Shenzhen, China. His research interests include rehabilitation robots, surgical robots, and motion assistance robots based on human-computer interaction for patients with limb movement disorders.



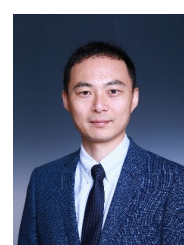
Chenglong Fu (Member, IEEE) is currently a Professor with the Department of Mechanical and Energy Engineering, Southern University of Science and Technology, Shenzhen, China. He has published more than 80 IEEE/ASME/Elsevier journal papers and more than 80 international conference proceedings. His research interests include wearable robots and physical human-robot interaction.



Bin Liang is currently a professor with the Department of Automation and the leading director of Institute of Navigation and Control. His research interests include robotics, intelligent control, etc. He is the vice Directing Member of China Society of Image and Graphics and was serving as the vice Directing Member of Chinese Society of Astronautics. He has authored and co-authored 2 books, 2 book chapters, 30 patents and more than 150 research papers.



Shiji Song (Senior Member, IEEE) received the Ph.D. degree in mathematics from the Department of Mathematics, Harbin Institute of Technology, Harbin, China, in 1996. He is currently a Professor with the Department of Automation, Tsinghua University, Beijing, China. He has authored more than 180 research papers. His current research interests include pattern recognition, system modeling, optimization, and control.



Xiang Li (Senior Member, IEEE) is currently an Associate Professor with the Department of Automation, Tsinghua University. His research interests include robotic manipulation, human-robot collaboration, control and planning, and micro/nano robots. He received the Best Application Paper Finalist in 2017 IROS and the Best Medical Robotics Paper Finalist in 2024 ICRA. He led the XL - Team and won the first place in 2024 ICRA Robotic Grasping and Manipulation Challenge (RGMC) In-hand Manipulation Track and also won the Most Elegant Solution across all the tracks. He has been serving as the Associate Editor of IEEE Robotics and Automation Letters since 2022, and also the Associate Editor of IEEE Transactions on Automation Science and Engineering since 2023. He is the Program Chair of the 2023 IEEE International Conference on Real-time Computing and Robotics.